Earthquake rupture through a step-over fault system: An exploratory numerical study of the Leech River Fault, southern Vancouver Island

Ge Li[1] and Yajing Liu[1]

[1]Department of Earth and Planetary Sciences, McGill University, Montreal, Québec, H3A 0E8, Canada

Key Points:

- Smaller offset distances, higher initial stresses and shallower fault burial depths promote rupture jumping across a step-over system.
- The joint influence of multiple parameters can be represented by the size of the Over Stressed Zone and the receiver fault stress state.
- Total maximum seismic moment grows with increasing Over Stressed Zone size.

Corresponding author: Ge Li, `ge.li2@mail.mcgill.ca`

Abstract

The Leech River fault (LRF) zone located on southern Vancouver Island is a major regional seismic source. We investigate potential interactions between earthquake ruptures on the LRF and the neighboring Southern Whidbey Island fault (SWIF), which can be interpreted as a step-over fault system. Using a linear slip-weakening frictional law, we perform 3D finite element simulations to study rupture jumping scenarios from the LRF (source fault) to the SWIF (receiver fault), focusing on the influences of the offset distance, fault initial stress level, and fault burial depth. We find a smaller offset distance, a higher initial stress level on either fault or a shallower fault burial depth will promote rupture jumping. Jumping scenarios can be interpreted as the response of the receiver fault to stress perturbations radiated from the source fault rupture. We demonstrate that the final rupture jumping scenario depends on various parameters, which can be collectively quantified by two keystone variables, the time-averaged Over Stressed Zone (where shear stress exceeds static frictional strength on the receiver fault) size $\overline{R_e}$ and the receiver fault initial stress level. Specifically, a smaller offset distance, a higher initial shear stress level, or a shallower burial depth will lead to a larger $\overline{R_e}$. The seismic moment on the receiver fault increases with increasing $\overline{R_e}$. When $\overline{R_e}$ reaches the threshold dependent on the receiver fault initial stress level, the rupture becomes break-away.

1 Introduction

Fault geometrical complexities can have a significant influence on earthquake ruptures. Two types of such geometrical complexities have been well documented by geological surveys and manifested in earthquake ruptures. One type is a main fault intersecting with a secondary, branch fault. For example, the 2002 M_w 7.9 Denali, Alaska, earthquake ruptured $\sim$ 220 km along the Denali fault before branching to and continuing on the Totschuda fault for another $\sim$ 75 km (Eberhart-Phillips et al., 2003; Bhat et al., 2004; Dunham & Archuleta, 2004). The second type is fault segmentation or step-over consisting of two or more discrete subparallel fault segments without clear surface signature of linkage (e.g. Sibson, 1986; Walsh et al., 2003; Wesnousky, 1988; Manighetti et al., 2009). In a fault step-over system, under certain conditions, rupture nucleated on one fault (the source fault) is nonetheless capable of jumping across the discontinuity and propagating onto the other fault (the receiver fault). This scenario may result in a longer rupture length and thus larger earthquake moment and magnitude (e.g. Harris

44   et al., 1991; Manighetti et al., 2007; Perrin, Manighetti, Ampuero, et al., 2016; Nissen

45   et al., 2016). Many large continental earthquakes tend to involve rupture propagating

46   across multiple fault segments. For example, the 2016 M_w 7.8 Kaikoura (New Zealand)

47   earthquake ruptured at least 12 individual fault segments (including stepovers of 15 -

48   20 km), with diverse faulting types and slip orientations, resulting in a total on land rup-

49   ture length of at least 170 km (Hamling et al., 2017; Cesca et al., 2017; Duputel & Rivera,

50   2017). Another prominent example of a multi-fault earthquake rupture is the 2019 Ridge-

51   crest earthquake sequence with a M_w 7.1 right-lateral mainshock triggered by a M_w 6.4

52   left-lateral foreshock (Liu et al., 2019). The primary structure ruptured during the main-

53   shock extends in the NW-SE direction and straddles the foreshock slip (Barnhart et al.,

54   2019; Liu et al., 2019) consisting of at least 20 faults (Ross et al., 2019).

55   The Kaikoura earthquake and the Ridgecrest earthquake highlight the limitations

56   of current seismic hazard models. Wesnousky (2006) examined the surficial ruptures of

57   22 historical earthquakes and showed a rupture will be terminated over an offset distance

58   of 5 km or larger. This threshold has been incorporated in the most well-developed earth-

59   quake rupture forecast model in California, the Uniform California Earthquake Rupture

60   Forecast 3 (UCERF3) model (Field et al., 2014), where the possibility of rupture jump-

61   ing across faults segments separated by a distance > 5 km is not considered. Accord-

62   ing to this model, the Kaikoura earthquake rupture, given the 10 - 15 km jumping dis-

63   tances in some step-overs, would not be considered as a plausible scenario (Hamling et

64   al., 2017). Moreover, both earthquakes ruptured many previously unmapped faults, ne-

65   cessitating the compilation of a more thorough fault database for seismic hazards assess-

66   ment. Such observations also emphasize the need to update existing seismic hazard as-

67   sessment studies which ignore the possibility of multiple-fault rupture in a known fault

68   system (Ross et al., 2019).

69   This need should be specifically recognized for the assessment of seismic hazards

70   posed by the Leech River fault (LRF), the major source of seismic hazard to the densely

71   populated areas in SW British Columbia , Canada (Zaleski, 2014; Morell et al., 2017;

72   Kukovica et al., 2019) (Figure 1). While the LRF is not yet included in the current seis-

73   mic hazard model used in the 2015 National Building Code of Canada (NBCC), its sig-

74   nificance as a major seismic hazard source has been recognized by several recent stud-

75   ies. The LRF serves as the lithologic contact separating the Crescent Terrane and the

76   Pacific Rim Terrane (MacLeod et al., 1977) and was imaged by seismic reflection stud-

ies as a $\sim 45°$ dipping structure (Clowes et al., 1987). It has been initially considered
as inactive due to lack of deformation since the Eocene (MacLeod et al., 1977). Recent
geomorphic (Morell et al., 2017, 2018) and seismic (Li et al., 2018) studies, however, pro-
vide strong evidence of Quaternary seismic activity. Based on Lidar detection and rang-
ing investigations, Morell et al. (2017) identified subparallel, steeply dipping topographic
features, and quaternary colluvium offset by a total of ~6 m, which collectively suggest
at least two M > 6 earthquakes have occurred along the LRF in the past $\sim 15,000$ years.
With Lidar observation and paleoseismic trenching studies, Morell et al. (2018) further
updated the proposition of LRF seismic activity to demonstrate that at least three earth-
quakes (M > 6) occurred along this fault within the last 9,000 years. Based on proba-
bilistic seismic hazard analysis, Kukovica et al. (2019) suggests that at a 2% probabil-
ity of exceedance in 50 years, the peak horizontal ground acceleration for the city of Vic-
toria will be increased by 9% to 0.63g from the current value of 0.58g due to inclusion
of a single active LRF. The activity of the LRF is complementarily supported by seis-
mic source property studies, including relocated hypocenters, event clustering, repeat-
ing events analysis, and focal mechanisms of earthquakes from 1992 to 2015 (Li et al.,
2018). Most of the earthquakes near the LRF are clustered along the segment east of
Leechtown, while the western segment exhibits seismic quiescence (Figure 1), consistent
with that morphology evidence is only observed along the eastern segment (Morell et al.,
2017). In addition, relocated seismicity by Li et al. (2018) clearly deviates from the seis-
mic active-source imaged lithologic contact (Clowes et al., 1987). Morell et al. (2017) also
made similar observations that identified fault planes and topographic scarps are not cor-
related with the lithologic surface traces. These data suggest the seismogenic structure
in this region is reactivated and do not reoccupy the lithologic contact. When incorpo-
rated with previous geological surveys, the seismicity distribution illustrates an 8 - 10
km wide, right-lateral, $\sim 60°$ NNE dipping fault zone along the eastern segment of the
mapped LRF surficial trace (Figure 1) (Li et al., 2018). Further offshore, shallow seis-
mic reflection and sediment core data suggests that the western extent of the Devil's Moun-
tain fault (DMF) connects with the LRF along the strike (Barrie & Greene, 2015), there-
fore we regard the DMF a part of this $\sim 60°$ NNE dipping fault structure.

The seismicity relocation study (Li et al., 2018) further suggests near the eastern
end of the NNE dipping LRF the existence of a separate, secondary structure, which is
probably an extension from the Southern Whidbey Island fault (SWIF), as also suggested

by previous studies (Johnson et al., 1999, 2001; Sherrod et al., 2008). Based on evidence presented above, the active structure in this region consists of both the LRF and the SWIF, which are separated a few kilometers apart. Since the DMF can be considered as a part of the LRF structure, we will not discuss it separately. As there is no strong evidence to constrain the SWIF geometry at depth nor the observations of its active fault trace near the LRF, we assume these two faults are parallel to each other and form a step-over fault system: the LRF to the north and the SWIF to the south. The simplified assumption of two parallel faults forming a step-over does not exclude the possibility that the SWIF strike is oblique to the LRF strike. If the two oblique fault traces do connect at depth, this would correspond to the case of a splay fault network (e.g. De Joussineau et al., 2007; Perrin, Manighetti, & Gaudemer, 2016), another common and important fault geometrical complexity. More data is required to consolidate either geometry configuration. Under the rupture scenario of an earthquake nucleated on the LRF jumping across the step-over and propagating onto the SWIF, the current SW British Columbia seismic hazard model would significantly underestimate the extent of potential damage. Motivated by the LRF-SWIF system, this work is a theoretical modeling study on rupture jumping scenarios in a step-over system. It should be emphasized that our model do not fully represent the LRF-SWIF system.

Previous numerical simulations of fault step-overs (e.g. Harris et al., 1991; Hu et al., 2016) demonstrate that earthquake rupture can jump across a step-over system under one of the following three scenarios: 1) a break-away rupture which propagates across the entire receiver fault surface, 2) a self-arresting rupture that propagates onto the receiver fault but stops shortly afterward and only ruptures part of it before stopping , or 3) no rupture jumping when the earthquake rupture stops at the source fault and fails to nucleate on the receiver fault. The break-away rupture is considered the most devastating as it produces the largest rupture size and seismic moment.

Whether earthquake ruptures can jump successfully across a step-over depends on a number of parameters, including the offset distance separating the source from the receiver fault (Harris & Day, 1999; Wesnousky, 2006; Hu et al., 2016), initial stress level on both faults (Hu et al., 2016), the free surface effect (Kase & Kuge, 2001; Hu et al., 2016), fault burial depth (Kase & Kuge, 2001), the abruptness of rupture termination (Oglesby, 2008), and frictional properties (Ryan & Oglesby, 2014; Lozos et al., 2014). A large offset distance impedes rupture jumping as stress perturbations radiated from

rupture on the source fault decays with distance. A higher initial stress level on the source fault can increases magnitude of stress perturbations during rupture propagation, while a higher initial stress level on the receiver fault increases its propensity to be triggered. Both factors contribute to promoting rupture jumping over the discontinuity. Besides, the Earth's surface, a traction-free boundary, can also promote rupture jumping as energy reflected from the free surface is capable of generating strong stress perturbations and sometimes supershear ruptures (Kase & Kuge, 2001; Chen & Zhang, 2006). Through a series of 3D simulations in a half-space model, Hu et al. (2016) found that the supershear rupture induced by the free surface can drive the rupture to jump over a distance > 10 km. They also report that rupture jumping distance significantly decreases with the fault burial depths (Kase & Kuge, 2001). Rupture is more capable of jumping across the step-over when it is terminated more abruptly on the source fault (Oglesby, 2008). The abruptness of rupture termination can be represented by coseismic slip decrease gradients near the boundary (Elliott et al., 2009). Fault frictional properties can also affect rupture jumping behaviors in a step-over system. Based on a linear slip-weakening law (Ida, 1972), where fault friction coefficient decreases linearly from a peak static value to a dynamic value with slip over a characteristic distance (See Equation 2 for details), Lozos et al. (2014) showed that the increase in the characteristic distance decreases rupture jumping distance. Ryan and Oglesby (2014) investigated the rupture processes of step-overs under various frictional laws including the linear slip-weakening law and different forms of the laboratory-derived rate and state friction law. Their study demonstrates that the functional forms of frictional laws play a significant role in controlling rupture jumping capability. In summary, we note that earthquake rupture jumping scenario is collectively dependent on a range of factors, despite all these previous modeling efforts on the influence of different single parameters. In this study, we focus on the influence of the offset distance, initial stress level, and burial depth.

Rupture on the source fault will radiate and impact stress perturbations on the receiver fault. While the radiated stress perturbations directly control rupture scenarios, target model parameters (i.e. offset distance, fault initial stress level, and fault burial depth) exert their influence indirectly by resulting in different stress perturbations on the receiver fault. To inspect the stress perturbations induced by the source fault rupture, previous studies on fault step-over systems (Harris et al., 1991; Harris & Day, 1993;

175   Fliss et al., 2005) propose the concept of stress difference $\Delta s(t)$:

176
$$\Delta s(t) = \mu_s \left| \sigma_{n0} + \Delta\sigma_n(t) \right| - \left| \tau_0 + \Delta\tau(t) \right| \qquad (1)$$

177   where μ_s is the static frictional coefficient, σ_{n0} is the initial normal stress, $\Delta\sigma_n(t)$ de-

178   notes the time-dependent normal stress perturbation, τ_0 is the initial shear stress and

179     $\Delta\tau(\text{t})$ denotes the time-dependent shear stress perturbation. Rupture can potentially

180   occur when and where the stress difference is less than zero. A more recent example is

181   from Hu et al. (2016), where they used $\Delta s(t)$ to explain that rupture jumping across dis-

182   tances greater than 10 km could only occur in lower normal stress cases with the free

183   surface effect considered. It is noteworthy that the stress perturbations presented in pre-

184   vious studies were first calculated in simulations consisting of a single source fault, and

185   then projected on a receiver fault plane in the step-over system. They considered that

186   rupture will nucleate on the receiver fault when and where $\Delta s(t) < 0$, but did not make

187   further quantitative assessments of whether the rupture will remain as self-arresting or

188   develop into a break-away one.

189   In this study, we present 3D finite-element simulations of the rupture process with

190   fault geometry motivated by the LRF step-over system. This is a numerical study de-

191   signed to explore potential rupture jumping scenarios under the influence of various tar-

192   get parameters and to facilitate understanding the physics process of fault interactions.

193   The first objective of this work is to study whether a rupture nucleated on the source

194   fault (LRF) will jump across the discontinuity and propagate onto the receiver fault (SWIF).

195   Compared to the LRF, the activity and geometry of the SWIF are poorly constrained

196   with no observed traces in this region. Therefore, we consider the LRF is more likely to

197   host the next large earthquake and study rupture propagating from the LRF instead of

198   from the SWIF. This contributes to the study of seismic hazards posed by the LRF, the

199   major structure in this region. We focus on the effect of offset distance, fault initial stress

200   level, and fault burial depth. The second objective is to identify keystone parameters that

201   can collectively represent the influence of the aforementioned variables and systemati-

202   cally study how they affect rupture jumping scenarios. This reduced degree-of-freedom

203   in the parameter space will provide a deeper understanding of this problem. Specifically,

204   we define the Over Stressed Zone (OSZ) as the region on the receiver fault plane with

205     $\Delta s(t) < 0$ and use it to predict rupture scenarios on the receiver fault. The OSZ can

206   be considered as an equivalence to the nucleation patch used to initiate an earthquake

207   rupture on the receiver fault. Similar to previous work on modeling dynamic earthquake

208 ruptures based on a linear slip-weakening law (Duan & Oglesby, 2006; Dalguer & Day,

209 2009; Galis et al., 2015; Xu et al., 2015; Harris et al., 2018), we conjecture that the vari-

210 ation of the OSZ size and the initial stress level on the receiver fault will have the most

211 critical influence on rupture evolution. We vary the values of target step-over parame-

212 ters and observe the change of the OSZ size resulted on the SWIF. We demonstrate that

213 the initial stress level on the receiver fault and the OSZ size can be used to represent the

214 joint influence of multiple model parameters. Seismic moment on the SWIF will grow

215 with increasing OSZ size, which after reaches a critical value dependent on the receiver

216 fault initial stress level, leads to break-away ruptures on the receiver fault.

2 Model Setup and Parameters

2.1 Step-over fault geometry, numerical method, and parameters

219 Figure 2 shows the geometrical parameters of the LRF step-over system. Previous

220 LRF seismicity relocation study (Li et al., 2018) provides some constraints on the LRF

221 geometry parameters, including its fault dimension and dipping angle. Relocated seis-

222 micity suggests that the seismically active part of the fault has a length of $L_1 = 50$ km,

223 extending to 30 km in depth with a dip angle of $\theta_1 = 60^o$, therefore its along-dip di-

224 mension is determined as $W_1 = 34.6$ km. The SWIF geometry, however, is relatively poorly

225 resolved. Relocated microseismicity studies (Li et al., 2018; Savard et al., 2018) indicate

226 that the SWIF could extend to 30 km in depth, but there is no information to decisively

227 determine its dip angle θ_2, length L_2, width W_2 as well as its offset distance L_0 from the

228 LRF. Other studies provide some insights that the SWIF should be considered as a fault

229 zone extending >150 km along strike from the Vancouver Island to the northern Puget

230 Lowland (Sherrod et al., 2008), and it is a steeply NNE dipping fault zone as wide as

231 6 - 11 km (e.g. Johnson et al., 1999). In this work, for simplicity, we consider the SWIF

232 segment in the proximity to the LRF with $\theta_2 = 90^o$, $L_2 = 30$ km and $W_2 = 30$ km. The

233 offset distance L_0 is varied from 1 to 10 km to study its effect on rupture jumping sce-

234 narios. The along-strike overlapping distance L is set as 10 km as relocated seismicity

235 suggests it falls within the range between 5 and 15 km.

236 As there is no definitive geological evidence on whether the LRF or the SWIF reaches

237 the surface, the possibility of faults with nonzero burial depths cannot be excluded. Con-

238 sidering surficial fault scarps observed along the LRF (Morell et al., 2017) and the abun-

239 dance of crustal LRF earthquakes at shallow depths <5 km (Li et al., 2018), it is rea-

240 sonable to assume the burial depth of the LRF (D_1) is relatively shallow. Since Li et al.

241 (2018) illustrate the SWIF lacks earthquakes shallower than 5 km, the burial depth of

242 the SWIF (D_2) is likely deeper than the LRF. We will vary D_1 within the range of [0,

243 1, 2] km and D_2 within the range of [0, 5, 10] km to study their effects. A complete list

244 of parameters discussed in this study and their values are included in Table 1.

245   We use Pylith, a finite-element code for 3D dynamic earthquake rupture simula-

246 tions (Aagaard et al., 2013) to investigate rupture process in the LRF step-over system.

247 We consider the LRF and the SWIF as two planar faults embedded in a homogeneous,

248 isotropic elastic half-space: P- and S- wave speeds are: $V_p = 6000$ m/s and $V_s = 3464$

249 m/s, Poisson's ratio $\nu = 0.25$, and shear modulus $G = 32$ GPa. Fault frictional prop-

250 erty is described by a linear slip-weakening law (Ida, 1972), where the frictional coeffi-

251 cient μ decreases linearly from a static value μ_s to a dynamic value μ_d with slip distance

252 δ over a characteristic slip-weakening distance d_0:

$$\mu(\delta) = \begin{cases} \mu_s - (\mu_s - \mu_d)\,\delta/d_0, & \delta \leq d_0 \\ \mu_d, & \delta > d_0 \end{cases} . \tag{2}$$

254 With these notations, static and dynamic shear stresses are thus defined as $\tau_s = \mu_s\sigma_{n0}$

255 and $\tau_d = \mu_d\sigma_{n0}$, respectively. The initial shear stress τ_0 can be represented using the

256 nondimensional value (Andrews, 1976):

$$S_0 = \frac{\tau_s - \tau_0}{\tau_0 - \tau_d} \tag{3}$$

258 A smaller S_0 indicates that the fault is closer to failure. It has been denoted that a suf-

259 ficiently small S_0 can induce break-away or even supershear ruptures in a full space model

260 (Xu et al., 2015). We assume a homogeneous distribution of initial shear stress on the

261 fault planes, except that the initial shear stress on the circular nucleation patch (τ_0^i) is

262 assumed to be slightly higher than the yielding strength (i.e. static shear stress τ_s) for

263 rupture initialization (Table 1). We use the same τ_0^i for the entire range of S_0, which is

264 considered appropriate as the results at lower S_0 are not biased (Figure S2). The nucle-

265 ation patch has a radius of 3 km and is located in the middle of the LRF along dip and

266 at 5 km from the left LRF boundary. In most cases considered in this study, we assume

267 that both fault segments in the step-over system have the same initial shear stress τ_0,

268 and use S_0 to represent the initial stress levels on both faults. We use S_0^{LRF} and S_0^{SWIF}

269 to discriminate S_0 on the LRF and the SWIF, if necessary, for example, when we inves-

tigate cases with different initial stress levels on two faults or we focus on the influence

of the initial stress level on the SWIF.

The cohesive zone size follows the definition in Day et al. (2005):

$$\Lambda_0 = \frac{9\pi}{32} \frac{G}{1-\nu} \frac{d_0}{\tau_s - \tau_d}. \tag{4}$$

$\Lambda_0 \approx 1.5$ km with parameter values chosen in our study (Table 1), which is about 10

times of the model grid size of 0.15 km, satisfying the numerical resolution requirement

(Day et al., 2005). To ensure computational stability, the computation time step Δt is

set to be much smaller than the time it takes for P wave to travel across the shortest grid

size. Besides, distorted tetrahedral grids in the mesh require smaller time steps due to

artificially high stiffness resulting from distorted shape (Aagaard et al., 2017). For a given

grid, the critical time step Δt_{cr} is derived from the formula given in Aagaard et al. (2017):

$$\Delta t_{cr} = \frac{\min(e_{\min}, C\frac{3V}{\sum_{i=1}^{4} A_i})}{V_p} \tag{5}$$

where e_{min} is the shortest grid size, V is the cell volume, A_i denotes the area of the ith

face, and C is the scaling factor empirically determined as 6.38 (Aagaard et al., 2017).

The global minima of Δt_{cr} is calculated to be 0.009 s. Therefore, time step Δt is set as

0.005 s in this study.

In our simulations, the fault edges are set as unbreakable boundaries except for the

free surface when $D_1 = 0$ km or $D_2 = 0$ km. Rupture fronts reaching the unbreakable

fault edges will be terminated abruptly. This abrupt termination will produce the high-

est co-seismic slip gradients that promote rupture jump across the step-over (Bernard

& Madariaga, 1984). Therefore, with all other conditions set equal, our unbreakable bound-

ary assumption represents the most likely condition for rupture jumping. We will dis-

cuss this boundary effect in further detail in Section 5.1.

2.2 Definition of Over Stressed Zone and design of numerical experiments

We will first inspect how different parameters of the step-over system will affect

the OSZ size observed on the SWIF. Following the convention used in previous studies

(e.g. Xu et al., 2015), we characterize the OSZ size using its effective radius $R_e(t)$:

$$R_e(t) = \sqrt{\frac{A(t)}{\pi}} \tag{6}$$

299 where A(t) is the cumulative area of grids where $\Delta s(t) < 0$. It is a function of time as

300 the OSZ results from both dynamic and static stress perturbations from the source fault.

301 Instead of analyzing the development history of $R_e(t)$, we take the time-averaged $\overline{R_e}$,

302 the mean of nonzero $R_e(t)$ values with the time window of $[t_1, t_2]$, as a representation

303 of the OSZ size for discussion in the following sections. t_1 is the time where the OSZ first

304 appears (for example $t_1 = 9$ s for $S_0 = 0.5$ in Figure S3) and t_2 is fixed at 25 s, when

305 the entire available area on the SWIF has been ruptured and seismic moment saturates

306 for all break-away ruptures (Figure S4). We use $\overline{R_e}$ to represent the OSZ size, but it should

307 be noted that $R_e(t)$ is time-dependent and its decay rate may also affect earthquake nu-

308 cleation on the receiver fault, particularly for cases with large L_0 where R_e decays fast

309 (Figure S5). The fast decay rate can be reflected in the smaller $\overline{R_e}$ observed. We also

310 ignore the influence of the OSZ shape, which can be important when the OSZ is very

311 irregular or elongated (Ripperger et al., 2007; Galis et al., 2019). This simplified repre-

312 sentation turns out to be appropriate as it agrees with the previous theoretical estimate

313 (as we show in Figure 11). We also tried the median and R_e^{max}, the maximum of $R_e(t)$.

314 It shows no significant difference for the median (Figure S6) and R_e^{max} turns out to be

315 an overestimate of the OSZ size (Figure S7).

316 Second, we investigate the effect of these parameters on rupture jumping scenar-

317 ios. To accomplish this, two sets of simulations are performed: 1) simulations consider-

318 ing the rupture on the single LRF, and 2) simulations considering ruptures on both faults

319 in the step-over system. In the first set, which can be referred to as the single LRF sim-

320 ulation set, we simulate dynamic ruptures on the single LRF (the only fault that rup-

321 ture is simulated), and project induced stress perturbation tensor on a hypothetical plane

322 with the same geometrical parameter as the SWIF. Rupture is not simulated on the hy-

323 pothetical plane and it only serves as a placeholder to receive the stress perturbations

324 induced by the LRF rupture. We define the OSZ as the region on the hypothetical plane

325 where stress difference $\Delta s(t) < 0$, and its area can be obtained by summing up all tri-

326 angular mesh surface areas satisfying $\Delta s(t) < 0$. This treatment allows us to focus on

327 the stress perturbations radiated from the source fault. In the second set, which can be

328 referred to as the step-over simulation set, we simulate dynamic earthquake ruptures in

329 the Leech River step-over system with both faults present and study the effects of dif-

330 ferent model parameters on the final SWIF rupture scenarios.

331   Through the implementation of two aforementioned simulation sets, we intend to

332 interpret the influence of different parameters on final rupture jumping scenarios, a re-

333 sponse represented by $\overline{R_e}$ on the SWIF with the initial stress level of S_0^{SWIF} to stress

334 perturbations radiated from the LRF. A theoretical estimate on the critical nucleation

335 size for break-away ruptures on an unbounded fault is developed by Galis et al. (2015):

$$R_{cr} = \frac{\pi}{4} \frac{1}{f_{\min}^2} \frac{\tau_s - \tau_d}{(\tau_0 - \tau_d)^2} G d_0 \tag{7}$$

337 where R_{cr} is the critical nucleation radius and $f_{\min}$ is the the minimum of the function

$$f(x) = \sqrt{x} \left[1 + \frac{\tau_0^i - \tau_0}{\tau_0 - \tau_d} (1 - \sqrt{1 - 1/x^2}) \right] \tag{8}$$

339 where τ_0^i is the initial shear stress within the nucleation patch and τ_0 and τ_d are the ini-

340 tial shear stress and dynamic shear stress defined outside of the nucleation patch. We

341 verify our numerical simulations against the theoretical estimates by simulating ruptures

342 on a single fault with the same geometry as SWIF through nucleation within a manu-

343 ally prescribed OSZ with a given R_{nuc} (here R_{nuc} is effectively the prescribed nucleation

344 zone size and it is considered as an initial condition instead of a function of time). Its

345 location is fixed at the fault plane center for simplicity. The consistency achieved between

346 this comparison (Figure 3) suggests that we can focus discussion on the influence of $\overline{R_e}$

347 and S_0^{SWIF} on SWIF rupture scenarios. It should be noted that Equation 7 is best suited

348 for configurations with $S_0 \geq 0.75$ and the theoretical estimate developed by Uenishi

349 (2009) has better performance for configurations with $S_0 \leq 0.75$. We use Equation 7

350 as an approximation for entire S_0 range with no significant deviations observed for $S_0 =$

351 $0.5-0.75$ on Figure 3. In addition to the initial shear stress level (represented by S_0),

352 Equation 7 suggests that R_{cr} also depends on the shear modulus G and characteristic

353 slip-weakening distance d_0, both of which are assumed to be constant in the model (G

354 $= 3.2$ GPa, $d_0 = 0.4$ m). In reality, faults are usually surrounded by fault damage zones

355 with lower shear modulus, leading to a smaller R_{cr}. It is more likely for ruptures to jump

356 across the discontinuity when the damage zones are considered (Finzi & Langer, 2012).

357 In addition, the characteristic slip weakening distance is not a well constrained param-

358 eter, with values ranging from 10^{-5} to 10^{-3} m determined by frictional experiments (Dieterich,

359 1978, 1979; Marone & Kilgore, 1993) and from 10^{-1} to 10^0 m determined from seismic

360 analysis (Ide & Takeo, 1997; Mikumo et al., 2003). Numerical simulations illustrate that

361 rupture jumping distance decays non-linearly with increasing d_0 (Lozos et al., 2014).

3 Simulation results

For the convenience of discussions in subsequent subsections, we will first describe how the OSZ on a hypothetical SWIF fault plane evolves with time as rupture develops on the LRF in Section 3.1. In Sections 3.2-3.4, we present the influence of different step-over parameters on the OSZ size and final jumping scenarios as the rupture is simulated on both faults.

3.1 Time evolution of OSZ on SWIF

Figure 4 shows the development of the OSZ resulted on a hypothetical SWIF fault plane for a simulation with initial shear stress level $S_0 = 0.7$ on both faults, offset distance $L_0 = 1$ km, and burial depths $D_1 = 0$ km and $D_2 = 0$ km. The initial rupture nucleated on the LRF is sub-shear. When the rupture front reaches the free surface, a supershear rupture is generated by the energy reflected from the free surface ($t = 9$ s in Figure 4a). These two rupture fronts are spatially separated due to different propagation speeds. In comparison, for a higher LRF initial stress level (lower $S_0 = 0.5$) with other parameters fixed, the initial rupture develops into a supershear rupture before reaching the free surface ($t = 4$ s in Figure 5a). When the initial rupture front meets the free surface, an additional supershear rupture is also generated, which is embedded in the initial rupture. It is clear from Figures 4b and 5b that the shape of the OSZ is irregular, and there could be multiple, separate OSZ patches simultaneously triggered on the receiver fault. In the following analysis, only $\overline{R_e}$ of the largest OSZ patch is considered, as a break-away rupture will be triggered as long as the largest OSZ reaches the critical size.

Figure 6 summarizes the time evolution of the effective size of the OSZ under the two initial stress levels for the cases in Figures 4 and 5. For a lower S_0, the OSZ starts to appear earlier (t $\sim$ 10 s) than the higher S_0 case (t $\sim$ 13 s). The OSZ also remains larger throughout the entire process, with the maximum $R_e(t)$ at ~ 3.5 km and ~ 2.5 km respectively. A higher initial stress on one fault segment in a step-over system provides more favorable conditions for nucleating ruptures on the other segment, with all other parameters held constant.

3.2 Influence of initial stress level

In this section, we focus on the effects of initial stress levels of LRF and/or SWIF on the size of the OSZ resulted on the SWIF. Here we fix the offset distance $L_0 = 1$ km, burial depths $D_1 = D_2 = 0$ km. Effects of these parameters will be examined in Sections 3.3 and 3.4. In general, we observe larger average OSZ size $\overline{R_e}$ at lower S_0 values. In other words, rupture is more likely to be nucleated on SWIF when the initial stress level is high (closer to static stress) on either or both of the LRF and SWIF faults. For example, as shown in the first panel of Figure 7, when the initial stress level is low ($S_0 >= 1.1$), $\overline{R_e}$ drops to a value significantly lower than R_{cr}. This can be directly compared with rupture jumping scenarios obtained in the step-over simulations (as we discuss in Section 3.5, see also Figure 10). Simulation results show that a break-away rupture cannot develop on the SWIF when $S_0 \geq 1.1$; rupture may propagate onto the SWIF but will get arrested shortly, indicating limited seismic hazards. The last two panels in Figure 7 illustrate the influence of initial stress level on one fault when S_0 on the other fault is fixed at 0.5. Based on these two panels, we can interpret the influence of S_0 in two aspects. First, a higher initial stress level on the SWIF leads to a smaller R_{cr} and a larger $\overline{R_e}$ (Figure 7), both encouraging rupture jumping across the discontinuity. Second, a higher initial stress level on the LRF will increases magnitude of stress perturbations and produce larger OSZs on the SWIF (Figure 7c).

3.3 Influence of offset distance

Figure 8 illustrates the influence of the offset distance between the LRF and the SWIF on the OSZ size resulted on the SWIF, at various initial stress levels. For each case, S_0 is assumed to be the same on both faults. This figure shows that $\overline{R_e}$ declines approximately linearly with the increase of L_0, demonstrating weaker stress perturbations the SWIF receives when the two faults are further apart. This is consistent with the results of the numerical experiment that a larger offset distance discourages the development of break-way ruptures (more discussion in Section 3.5, see also Figure 10) when other parameters are fixed. We define the maximum jumping distance as the largest offset distance that allows a self-arresting rupture on the SWIF, and the critical jumping distance as the largest offset distance that allows a break-away rupture on the SWIF. Rupture jumping distance reaches its maximum of 8 km when the SWIF has sufficient proximity to its failure (low $S_0 = 0.5$) and the LRF reaches the free surface ($D_1 = 0$ km

in Figures 10a-10b). For simulations with $S_0 = 0.7$, $D_1 = 0$ km, and $D_2 = 0$ km, $\overline{R_e}$ drops below the corresponding R_{cr} when L_0 increases to 3 km or larger (Figure 8). The shrinkage of OSZ with increasing offset distance results in a critical jumping distance of 2 km (Figure 10a).

A previous numerical study (Hu et al., 2016) suggests that the critical jumping distance can reach up to 14 km, significantly exceeding the largest critical jumping distance of 6 km obtained in this work ($S_0 = 0.5$, $D_1 = 0$ km and $D_2 = 0$ km in Figure 10a). This discrepancy can be attributed to two factors. First, they used a higher initial stress level of $S_0 = 0.4$, which facilitates rupture jumping as well as the development of break-away ruptures. Second, the acceleration length of rupture front (ALRF) on the source fault prior to rupture jumping—the distance between the source fault nucleation patch and its fault edge in the proximity of the step-over—used in Hu et al. (2016) is 34 km, larger than the ALRF of 20 km used in our work. A larger ALRF leads to higher slip gradients on the source fault, hence stronger stopping phases and a larger critical jumping distance (Oglesby, 2008; Elliott et al., 2009).

3.4 Influence of fault burial depth

The influence of fault burial depth (i.e. D_1 and D_2) on $\overline{R_e}$ is demonstrated in Figure 9. Overall we observe the strongest perturbation effects when both faults reach the free surface. The OSZ size decreases with the burial depths of either fault. When the LRF is a blind fault ($D_1 > 0$), the energy reflected by the free surface diminishes as the burial depth increases, resulting in weaker stress perturbations and smaller OSZs on the SWIF. The weakening of stress perturbation radiated on the SWIF is also observed when increasing D_2 while keeping $D_1 = 0$ km. It takes effect in a different way than increasing D_1: a nonzero D_1 weakens the stress perturbations from the source side while a nonzero D_2 weakens the stress perturbations from the receiver side. It can also be speculated from Figure 9 that the effect of a larger D_1 can be compensated by a smaller D_2. Thus, it may be problematic to predict the jumping scenario by measuring the burial depth of either the source fault or the receiver fault alone. For a given D_1, $\overline{R_e}$ keeps decreasing with the deepening of the receiver fault burial depth—D_2, indicating stress perturbations radiated on the receiver fault is a near-surface effect. The OSZ may be completely diminished when the receiver fault is too deep even the source fault rupture reaches the free surface. The effect of nonzero D_2 in impeding rupture jumping, however, is much

less effective compared to D_1. Figures 10a - 10b show the earthquake rupture is still capable of jumping over a distance of 8 km when D_2 increases to 5 km with other parameters fixed as $L_0 = 1$ km, $S_0 = 0.5$, and $D_2 = 0$km. Figure 5b shows the OSZ developed on the SWIF can extend down to about 12 km (the snapshot at t = 18 s in Figure 5b), indicating the SWIF earthquake will be triggered when D_2 is shallower than this depth. Several factors may influence the free surface effect and consequently change the influence of fault burial depths on rupture jumping scenarios. We assume a uniform distribution of initial normal stress in this study, but the normal stress is more realistic to be depth-dependent. Kaneko and Lapusta (2010) suggest that the free surface effect will be more profound with lower normal stresses near the surface. In this case, break-away ruptures can be generated with smaller OSZ sizes or at greater burial depths. Besides, many studies suggest the presence of rate-strengthening friction at shallow depths. For example, laboratory experiments showed that unconsolidated fault gouge leads to rate-strengthening friction behavior at shallow depths (Marone, 1998). The rate-strengthening effect would stabilize rupture, in competition with the rupture updip propagation. Relatively, this region will serve as a stronger barrier impeding rupture development. Kaneko et al. (2008) showed that the rate-strengthening region at shallow depth will suppress the free surface effect. A larger OSZ size may be required to produce a break-away rupture on the receiver fault.

3.5 Simulation results summary

The general messages delivered in Figures 6-9 are: 1) the OSZ enlarges to its peak size a few seconds after its first appearance and shrinks gradually; and 2) higher initial stress levels, closer offset distances and shallower fault burial depths produce larger OSZs on the receiver fault. These messages are consistent with the phase diagrams showing the influence of different parameters on final rupture scenarios in Figure 10. It is illustrated clearly that higher initial stress levels, smaller offset distances, or shallower fault burial depths will promote successful rupture jumping and the transition of self-arresting ruptures into break-away ones. The final rupture jumping scenario depends on the collective influence of various model parameters, which can be interpreted by inspecting how they change $\overline{R_e}$ on the SWIF and whether $\overline{R_e}$ reaches R_{cr}. The phase diagrams in Figure 10 can be useful to predict final rupture jumping scenarios with given parameter values. We show selected combinations of D_1 and D_2 in the phase diagrams as the scenar-

ios are more sensitive to model parameters for burial depth within this range. Based on relocated seismicity (Li et al., 2018), it is most likely that the SWIF has a burial depth of $D_2 = 5$ km and the offset distance $L_0 = 5$ km. Based on Figure 10b, it can be inferred that a rupture nucleated on the LRF is unlikely to jump across the step-over even when the LRF rupture reaches the free surface ($D_1 = 0$ km) unless the two faults are critically stressed ($S_0 = 0.5$).

From the initial comparative simulations with a single SWIF in Section 3, we obtain the data of the final seismic moment on the SWIF (M_0^{SWIF}) as a function of R_{nuc} for different initial stress levels, which we denote as the (R_{nuc}, M_0^{SWIF}) data set. We then obtain the data of the OSZ development history (represented by $\overline{R_e}$) resulting from the single LRF simulation set and seismic moment on the SWIF (M_0^{SWIF}) resulting from the step-over simulation set, which we denote as the ($\overline{R_e}$, M_0^{SWIF}) data set. We create Figure 11 by combining these two data sets, intending to compile and compare the results of different simulation sets. Both data sets follow the trend that : 1) a larger R_{nuc} or $\overline{R_e}$ leads to a larger M_0^{SWIF}; and 2) when R_{nuc} or $\overline{R_e}$ reaches a critical value, the SWIF rupture becomes break-away and its seismic moment increases up to a saturated value depending on the available rupture area of the receiver fault. The observation that rupture sizes increase with nucleation zone size is consistent with previous numerical studies (e.g. Galis et al., 2017). The critical value for both R_{nuc} and $\overline{R_e}$ can be estimated by Equation 7 and illustrated by a vertical dashed line for each S_0 case in Figure 11. The consistency in Figure 11 demonstrates that $\overline{R_e}$ and S_0^{SWIF} are the keystone variables directly controlling final rupture jumping scenarios in a step-over fault system, while different parameters exert their influence on rupture scenarios by resulting in different OSZ sizes.

4 Research implications

4.1 Seismic hazards assessment

This study reveals potential limitations of previous LRF seismic hazard studies based on ground motion simulations (Molnar et al., 2014) and probabilistic seismic hazard analysis (Kukovica et al., 2019), which only consider the influence of a single LRF. Figure 12a shows, if an earthquake propagates across the offset and continues onto SWIF as a break-way rupture(for example as in the case of $S_0 = 0.5$, $S_0 = 0.7$ and $S_0 = 0.9$), the

final seismic moment could increase by 25%. In an observational study on the 1997 M_w

7.1 Harnai (Pakistan) earthquake (Nissen et al., 2016), the eventual seismic moment is

increased by 50% due to the successive rupture triggered on the receiver fault by the source

fault rupture. Fault models derived by Nissen et al. (2016) using InSAR data suggest

that the surface projection of these two faults is parallel with an offset distance of ~ 5

km. This study demonstrates the importance of considering the possibility of rupture

jumping for regional seismic assessment. M_0^{SWIF} released by a self-arresting rupture on

the SWIF ($S_0 = 1.1$ and $S_0 = 1.3$) is negligible therefore not shown in Figure 12a. The

moment release rate ($\dot{M}_0$) as a function of time in Figure 12b displays more details on

the energy release history, which highlights the difference between a self-arresting rup-

ture and a break-away one. The $\dot{M}_0$ curves for self-arresting ruptures (dashed lines) are

single-peaked while the $\dot{M}_0$ curves for break-away ruptures (solid lines) have double peaks.

The second peak represents the successive fault rupture on the SWIF. Similar patterns

of multiple $\dot{M}_0$ pulses have been observed in several multi-fault earthquakes for exam-

ple the 1997 Harnai earthquake (Nissen et al., 2016) and the 2016 Kaikoura earthquake

(Hollingsworth et al., 2017).

In the state-of-the-art rupture forecasts model in California—UCERF3 (Field et

al., 2014), the possibility of rupture jumping between fault segments separated by a dis-

tance > 5 km is not considered. This assumption, however, is not definitively solid as

the sequential failure of two faults with offset distance larger than 5 km could happen

under many conditions, e.g., when the receiver fault is critically-stressed, or the free sur-

face effect is strong enough. Therefore, the seismic hazards of a step-over fault system

such as the LRF-SWIF can be significantly underestimated if the possibility of jump-

ing distance > 5 km is neglected.

Furthermore, it is questionable to rely on the offset distance alone to judge whether

an earthquake will jump across the discontinuity. First, whether an earthquake rupture

jumps across the discontinuity is a collective result depending on a variety of model pa-

rameters. In addition to the parameters investigated in this study (L_0, S_0, D_1, D_2), it

is also dependent on many other factors that are not modeled in thi study, for example,

the presence of secondary faults and cracks in the step-over and mechanical properties

of the step-over. Second, the offset distance is not always observable especially when there

is a lack of the observation of surficial fault scarps. Based on seismicity relocation and

finite fault slip model, Ross et al. (2019) determined that the 2019 Ridgecrest earthquake

ruptured multiple crustal faults with significant geometrical complexity. Most of the faults ruptured in this earthquake sequence are not mapped in previous fault databases.

4.2 Aftershock pattern predictions

It has been a common practice to relate near-field aftershock distributions or seismicity triggering with static stress changes due to permanent displacement (e.g. Das & Scholz, 1981; Toda et al., 1998; Verdecchia et al., 2018). In a broader sense, aftershock triggering mechanism can be treated as a problem of stress transfer from the primary fault to micro-faults in the proximity. Our findings, especially the transient properties of the OSZ, highlight the non-negligible effects of dynamic stress changes in the near-field. Aftershocks could also be triggered in a stress shadow zone—regions with zero or negative static stress changes, as long as the transient dynamic stress perturbations are capable of bringing it to failure (Kilb et al., 2000, 2002; Voisin et al., 2004; Freed, 2005). Besides, separating dynamic and static stress changes in the near-field is impossible. In terms of triggering aftershocks, it has been shown that dynamic stress changes can be equally significant as static stress changes (Kilb et al., 2002). Voisin et al. (2004) suggest the complete Coulomb failure function, a combination of static and dynamic stress changes, should be considered to explain seismicity triggering mechanisms and aftershock patterns.

5 Discussion

5.1 Stopping phases

Previous numerical results (Oglesby, 2008) illustrate that the possibility of rupture jumping is suppressed when reducing the gradients of the initial shear stress distribution near the fault boundary. Moreover, through the analysis of historical large-magnitude earthquakes, Elliott et al. (2009) reveal that it is unlikely for a rupture to propagate onto the next segment for earthquakes with low slip gradients near the step-overs. A rupture is less capable of jumping across the discontinuity when faults are terminated more gradually. Both studies recognize the indispensability of seismic energy from the stopping phases in promoting earthquake jumping across the step-over. We simply assume rupture is terminated abruptly in this study as there are no data to constrain fault bound-

ary conditions. Therefore, our assumption of abrupt fault termination results in the highest coseismic slip gradient and hence promotes rupture jump across the step-over.

As shown in Figures 4 and 5, the OSZ starts to develop after the right-ward propagating LRF rupture reaches the right fault edge in the proximity of the step-over. The vertical red dashed lines in Figure 6 represent when the LRF rupture fronts meet the fault edge in the proximity of the step-over for the simulation case in Figure 4 (simulation snapshots at t = 12 s and t = 13.7 s). Curves for $S_0 = 0.7$ in Figure 6 include two pulses, representing the energy from the termination of two rupture fronts, respectively. These transient properties serve as an indicator of the passage of stopping phases and its role in radiating stress perturbations on the SWIF.

Rupture propagation of 2 selected simulations is included in the supplementary materials as Movies S1 - S2. Rupture on the SWIF starts to propagate after the source fault rupture front reaches the right edge of the LRF, an unbreakable boundary halting rupture propagation. This indicates the strong effect of stopping phases. Movies S1 - S2 also show that the SWIF hypocenter is about 10 km from its left boundary, which corresponds to the projection of the LRF right fault boundary on the SWIF surface. King et al. (1994) calculated the static stress changes due to the slip on a right-lateral master fault in an extensional step-over system. Their study suggests that, for a right-lateral fault with a strike parallel to the source fault, positive Coulomb stress changes are distributed in the proximity of the source fault boundary, which is consistent with our observations on the SWIF hypocenter location and the observations in other numerical experiments (e.g. Harris et al., 1991; Harris & Day, 1993).

However, observations on many fault systems suggest smooth rupture terminations near the fault boundary. Surficial field mapping of the 1992 Landers earthquake (McGill & Rubin, 1999) indicates that fault slip can decrease from a few meters to zero over a distance about 1 km. Slip inversions often suggests even smoother gradients of fault slip decreasing to zero over a distance > 5 km (Ozacar & Beck, 2004). For faults with evidence suggesting more gradual termination at the boundaries, rupture jumping across the discontinuity is expected to be less likely. In this study, the assumption of abrupt fault termination represents, with all other conditions set equal, the highest likelihood scenario promoting rupture jump across the step-over.

5.2 Fault stress level initialization

The initialization of shear stress on the fault is a crucial component of a dynamic rupture simulation study. For simplicity, we assume a uniform distribution of initial stress across two planar faults (Harris et al., 1991; Kase & Kuge, 2001; Xu et al., 2015; Weng & Yang, 2017), except for the stress asperity implemented to initialize the rupture. While the reduced complexity allows us focus on target parameters, previous studies have shown the undeniable significance of other stress initialization strategies: 1) regional tectonic stress strategy (Fliss et al., 2005; Bhat et al., 2007); 2) fault roughness strategy (Dunham et al., 2011; Mai & Beroza, 2002); and 3) evolved stress strategy (Stern, 2016; Tarnowski, 2017).

In Fliss et al. (2005) and Bhat et al. (2007), regional tectonic stress tensor is resolved onto the fault plane according to local surface normal orientations. This strategy can be used to inspect the fault's geometrical effects. Based on an observation of the orientation $S_{H_{\max}}$, a stress tensor is created with the assumption of a σ_1 direction and S_0.

Besides, observational studies suggest that fault roughness exists at all scales across the surface (Dunham et al., 2011; Mai & Beroza, 2002) in the aspect of heterogeneous fault asperities strength distributions and fault surface non-planarity. Fault roughness has been demonstrated to constitute a fundamental factor of the rupture process (e.g. Mai & Beroza, 2002; Brodsky et al., 2016). Some studies suggest that the heterogeneous static stress field for faults and earthquake slips is not fully stochastic but rather showing certain patterns (e.g. Manighetti et al., 2005, 2015). Other studies approximate this factor by a stochastic heterogeneous stress field applied on the fault plane (e.g. Ripperger et al., 2007; Zielke et al., 2017). The variation of the stress field deviation can results in a sharp increase in earthquake sizes (Ripperger et al., 2007). In Zielke et al. (2017)'s numerical simulations, it is shown that the release of seismic moment can vary widely depending on the roughness and the location of strength asperities. Their study shows that faults with higher roughness may produce smaller earthquakes under identical loading conditions.

Moreover, in our 3D dynamic simulations, we ignore the process of stress loading on the faults. It is suggested that a more realistic initial stress distribution for dynamic simulations can be constructed from the stress outputs from quasi-static crustal mod-

eling (Stern, 2016; Tarnowski, 2017) or from the geodetic loading conditions (Yang et al., 2019). But this strategy requires rigorous pre-calculations of the fault stress evolution history in designated study areas. The lack of necessary observations, e.g., fault roughness data and stress evolution history, prevents us from implementing other strategies. In addition, the implementation of the regional stress tensor strategy becomes unnecessary as the influence of fault geometrical irregularities is currently beyond the scope of this study. When data is available, our work can be expanded to investigate the influence of these factors on the rupture process in a step-over system.

5.3 Fault geometry

In this study we assume the SWIF is a vertical fault parallel to the LRF. The SWIF geometry, however, is poorly constrained without strong geologic and seismic evidence. It could be a splay fault developed as the LRF grows (De Joussineau et al., 2007; Perrin, Manighetti, & Gaudemer, 2016; Perrin, Manighetti, Ampuero, et al., 2016) with a different strike orientation. Considering a constant loading stress tensor in this region, the initial stress field resolved on the receiver fault will be dependent on fault strike and surface normal orientations. Moreover, as rupture propagates, the resolved stress on the receiver fault also depends on the relative geometry between two faults. For example, if the SWIF has a similar dipping angle to the LRF, the fault planes are effectively closer given the same offset distance (distance between the surface traces of the source fault and receiver fault). This may result in larger OSZs with the same nominal offset distance. In addition, the free surface has slightly weaker effects on the rupture process on vertical faults, as it lacks multiple reflections of seismic waves between the free surface and the fault plane (Xu et al., 2015). Our study is a generic numerical modeling investigation on a subparallel fault step-over system motivated by limited observations from the LRF-SWIF fault system. Main findings on the variation of $\overline{R_e}$ according to target parameters and its influence on rupture jumping scenarios still hold, but we acknowledge that adjustment in some aspects of the model setup is needed if additional observational constraints become available.

5.4 Representation of the OSZ size

The key concept developed in this study is the OSZ size, which is given by the effective radius $R_e(t)$ in Equation 6. In subsequent analysis, we use $\overline{R_e}$, the time-averaged

value to represent the overall OSZ size over its evolution history. The similar trend observed for the ($\overline{R_e}$, M_0^{SWIF}) dataset and the (R_{nuc}, M_0^{SWIF}) dataset in Figure 11 suggests this treatment is appropriate. However, some discrepancies should be noted: the critical $\overline{R_e}$ for a break-away rupture jumping is not exactly R_{cr}. We speculate that these discrepancies can be attributed to several factors. First, the OSZ radiated on the SWIF in a step-over system usually reaches the free surface (Figures 4b and 5b) while the nucleation zone used in the single SWIF simulation set is located at the center of the fault plane. The influence of the free surface effect on the(R_{nuc}, M_0^{SWIF}) dataset is relatively weaker, especially when the rupture in the comparative simulations does not expand to the free surface with a small R_{nuc}. This may be accountable for that the earthquake rupture in the ($\overline{R_e}$, M_0^{SWIF}) dataset produces slightly higher seismic moments and can develop into a break-away rupture with a relatively smaller OSZ size than the (R_{nuc}, M_0^{SWIF}) dataset (Figures 11a and 11c). Second, the definition of R_e in Equation 6 assumes the OSZ is a circular patch, while Figures 4b and 5b show that it is irregular with an elongated shape. For irregular OSZs, the OSZ size should be corrected with a critical compact region in addition to the size of the area (Ripperger et al., 2008). For elongated OSZs, the instability is not controlled by the area of the OSZ but by its shorter dimension (Galis et al., 2019). For some selected cases, we fit the OSZ by a 95% confidence ellipse and obtain its major and minor axis length ratio (Figure S8) and the inclination angle θ (Figure S9), i.e. the angle between the major axis and the horizontal axis. θ is relatively stabilized at about 70°. The aspect ratio varies over time and it does not exceed 3.5 with a median of about 2.2 for selected cases. This may suggest the OSZ should be treated as elongated according to Galis et al. (2019). Third, the amplitude of stress difference Δs inside the OSZ is not uniform, while the determination of R_{cr} assumes a uniform distribution of Δs. Finally, we only consider the largest OSZ patch, which may underestimate the OSZ size as other smaller patches can also contribute to the rupture development on the SWIF.

5.5 Fault maturity

Fault maturity, a state depending on fault age, length, slip and slip rate (Perrin, Manighetti, Ampuero, et al., 2016), defines the evolution state of fault structural properties. It plays a key role impacting fault zone geometrical, mechanical (Perrin, Manighetti, Ampuero, et al., 2016; Manighetti et al., 2007) and frictional (Marone & Kilgore, 1993;

Savage & Cooke, 2010) properties and thus earthquake behaviours and its possibility of jumping across discontinuities. Perrin, Manighetti, Ampuero, et al. (2016) analyzed the slip distributions of 27 large continental earthquakes and showed that the largest earthquake slip and rupture speed on each fault occurred on segments with the highest maturity. As suggested by natural fault data, discrete segments of a fault system can gradually coalesce into a throughgoing fault when the fault displacement accumulates (Wesnousky, 1988; Manighetti et al., 2015). As faults mature, off-fault damage zones form and develop from repeated fault deformation and displacement (e.g. Cooke, 1997; Manighetti et al., 2004; Savage & Brodsky, 2011). Dynamic simulations considering plastic responses to fault slips (Ma & Andrews, 2010) suggest that the off-fault damage tends to be confined in a narrow region around the fault and this damage zone broadens when the off-fault material cohesion decreases. Damaged zones can result in seismic velocity reductions up to 60% for both compressional and shear waves around the fault (Huang et al., 2014). As suggested by Equation 7, a lower shear modulus (as a result of seismic velocity reductions) in the fault damaged zone will lead to a smaller critical nucleation size. Therefore it will be easier for ruptures to jump across the discontinuity. Numerical experiments suggest that it is more likely for a rupture nucleated in the fault damage zone to develop into a break-away rupture when the fault is maturer (Huang, 2018). Moreover, Finzi and Langer (2012) showed that shear modulus reductions in a fault damaged zone can greatly increase the jumping distance, indicating a higher possibility of large cascading earthquakes. In addition to mechanical properties, fault maturity can also influence the frictional properties. Marone and Kilgore (1993) suggested the critical slip distance, the slip distance it takes for friction to evolve into a new steady-state value, increases with the width of fault gouges. This finding indicates that a maturer fault, presumably with more gouge materials, may have a larger characteristic slip weakening distance d_0. In a 2D finite-element study, Lozos et al. (2014) showed that increasing d_0 suppresses the capability of an earthquake rupture jumping across the step-over, as it increases the critical nucleation zone size on the receiver fault (Equation 7). Studies discussed above suggest that the existence of a damaged zone can introduce two factors— shear modulus reduction and d_0 increase—on rupture development. Since the critical nucleation zone size is directly proportional to both the shear modulus and d_0 (e.g. Day et al., 2005; Galis et al., 2015; Huang et al., 2014), these two factors will compete against

738   each other. Future work may be required to inspect the joint influence of these two fac-

739   tors as functions of fault maturity.

6   Conclusions

741   Recent geomorphic and seismic studies of the Leech River Fault zone have started

742   to recognize its potential as a prominent seismic hazard source to nearby populated re-

743   gions in southwest British Columbia, Canada (Halchuk et al., 2019). Relevant studies

744   (Johnson et al., 1999, 2001; Sherrod et al., 2005, 2008; Morell et al., 2017, 2018) suggest

745   that the LRF and the SWIF constitute a complex crustal fault system and potential fault

746   interactions during an earthquake rupture may lead to greater damages than previously

747   assessed. As a numerical modeling study, this work aims to explore potential fault in-

748   teractions during a hypothetical LRF earthquake. As there is no strong evidence to con-

749   strain the SWIF geometry, we assume the LRF and the SWIF are parallel to each other

750   and form a step-over fault system. With this assumption and many others, this study

751   provides a detailed investigation on the influence of various target parameters on whether

752   a rupture nucleated on the LRF can jump across the discontinuity and propagate onto

753   the SWIF. The parameters we focus on are the offset distance (L_0), fault initial stress

754   level (S_0), and burial depth (D_1 or D_2). We find a smaller offset distance, a higher ini-

755   tial stress level on either fault or a shallower fault burial depth will promote a success-

756   ful rupture jumping. Our study shows that the seismic hazards posed by the LRF sys-

757   tem could be significantly higher than previously estimated, especially under the scenario

758   when the earthquake nucleated on the LRF jumps onto the SWIF as a break-away rup-

759   ture.

760   In a broader sense, our study also contributes to understanding the physics of multi-

761   fault interaction. Whether a rupture propagates onto another individual fault segment

762   and whether it develops into a break-away or self-arresting rupture depends on the col-

763   lective effects of a variety of parameters. Therefore, it may be not always feasible to pre-

764   dict whether rupture jumping is possible based on a single parameter. Instead, we pro-

765   pose and verify through dynamic rupture simulation that the final rupture jumping sce-

766   narios can be interpreted as the response of the receiver fault to stress perturbations ra-

767   diated from the source fault rupture. This effect of stress perturbations can be quanti-

768   fied using the time-averaged Over Stressed Zone (OSZ) size—$\overline{R_e}$. We find $\overline{R_e}$ and the

769   receiver fault initial stress level are the keystone variables that can represent the collec-

tive influence of various parameters. Specifically, a smaller offset distance, a higher initial shear stress level, or a shallower burial depth will lead to a larger $\overline{R_e}$. The seismic moment on the receiver fault increases with increasing $\overline{R_e}$. When $\overline{R_e}$ reaches the critical value that depends on the receiver fault initial stress level, the rupture becomes breakaway and its seismic moment increases up to a saturated value depending on the total available area of the receiver fault.

Acknowledgments

References

Aagaard, B. T., Knepley, M. G., & Williams, C. A. (2013). A domain decomposition approach to implementing fault slip in finite-element models of quasi-static and dynamic crustal deformation. *Journal of Geophysical Research: Solid Earth*, *118*(6), 3059–3079.

Aagaard, B. T., Knepley, M. G., & Williams, C. A. (2017). Pylith user manual, version 2.2.1. davis, ca: Computational infrastructure of geodynamics.

Andrews, D. (1976). Rupture velocity of plane strain shear cracks. *Journal of Geophysical Research*, *81*(32), 5679–5687.

Barnhart, W. D., Hayes, G. P., & Gold, R. D. (2019). The July 2019 Ridgecrest, California, Earthquake Sequence: Kinematics of Slip and Stressing in Cross-Fault Ruptures. *Geophysical Research Letters*, *46*(21), 11859–11867.

Barrie, J. V., & Greene, H. G. (2015). *Active faulting in the northern juan de fuca strait: implications for victoria, british columbia.* Natural Resources Canada.

Bernard, P., & Madariaga, R. (1984). A new asymptotic method for the modeling of near-field accelerograms. *Bulletin of the Seismological Society of America*, *74*(2), 539–557.

Bhat, H. S., Dmowska, R., Rice, J. R., & Kame, N. (2004). Dynamic slip transfer from the Denali to Totschunda faults, Alaska: Testing theory for fault branching. *Bulletin of the Seismological Society of America*, *94*(6B), S202–S213.

Bhat, H. S., Olives, M., Dmowska, R., & Rice, J. R. (2007). Role of fault branches in earthquake rupture dynamics. *Journal of Geophysical Research: Solid Earth*, *112*(B11).

Brodsky, E. E., Kirkpatrick, J. D., & Candela, T. (2016). Constraints from fault roughness on the scale-dependent strength of rocks. *Geology*, *44*(1), 19–22.

Cesca, S., Zhang, Y., Mouslopoulou, V., Wang, R., Saul, J., Savage, M., . . . Dahm, T. (2017). Complex rupture process of the Mw 7.8, 2016, Kaikoura earthquake, New Zealand, and its aftershock sequence. *Earth and Planetary Science Letters*, *478*, 110–120.

Chen, X., & Zhang, H. (2006). Modelling rupture dynamics of a planar fault in 3-D half space by boundary integral equation method: An overview. *pure and applied geophysics*, *163*(2-3), 267–299.

Clowes, R., Brandon, M., Green, A., Yorath, C., Brown, A. S., Kanasewich, E., & Spencer, C. (1987). Lithoprobe—southern vancouver island: Cenozoic subduction complex imaged by deep seismic reflections. *Canadian Journal of Earth Sciences*, *24*(1), 31–51.

Cooke, M. L. (1997). Fracture localization along faults with spatially varying friction. *Journal of Geophysical Research: Solid Earth*, *102*(B10), 22425–22434.

Dalguer, L. A., & Day, S. M. (2009). Asymmetric rupture of large aspect-ratio faults at bimaterial interface in 3D. *Geophysical Research Letters*, *36*(23).

Das, S., & Scholz, C. H. (1981). Off-fault aftershock clusters caused by shear stress increase? *Bulletin of the Seismological Society of America*, *71*(5), 1669–1675.

Day, S. M., Dalguer, L. A., Lapusta, N., & Liu, Y. (2005). Comparison of finite difference and boundary integral solutions to three-dimensional spontaneous rupture. *Journal of Geophysical Research: Solid Earth*, *110*(B12).

De Joussineau, G., Mutlu, O., Aydin, A., & Pollard, D. D. (2007). Characterization of strike-slip fault–splay relationships in sandstone. *Journal of Structural Geology*, *29*(11), 1831–1842.

Dieterich, J. H. (1978). Time-dependent friction and the mechanics of stick-slip. In *Rock friction and earthquake prediction* (pp. 790–806). Springer.

Dieterich, J. H. (1979). Modeling of rock friction: 1. experimental results and constitutive equations. *Journal of Geophysical Research: Solid Earth*, *84*(B5), 2161–2168.

Duan, B., & Oglesby, D. D. (2006). Heterogeneous fault stresses from previous earthquakes and the effect on dynamics of parallel strike-slip faults. *Journal of Geophysical Research: Solid Earth*, *111*(B5). doi: 10.1029/2005JB004138

Dunham, E. M., & Archuleta, R. J. (2004). Evidence for a supershear transient during the 2002 Denali fault earthquake. *Bulletin of the Seismological Society of America*, *94*(6B), S256–S268. doi: 10.1785/0120040616

Dunham, E. M., Kozdon, J. E., Belanger, D., & Cong, L. (2011). Earthquake ruptures on rough faults. In *Multiscale and multiphysics processes in geomechanics* (pp. 145–148). Springer.

Duputel, Z., & Rivera, L. (2017). Long-period analysis of the 2016 Kaikoura earthquake. *Physics of the Earth and Planetary Interiors*, *265*, 62–66.

Eberhart-Phillips, D., Haeussler, P. J., Freymueller, J. T., Frankel, A. D., Rubin, C. M., Craw, P., . . . others (2003). The 2002 Denali fault earthquake, Alaska: A large magnitude, slip-partitioned event. *Science*, *300*(5622), 1113–1118.

Elliott, A., Dolan, J., & Oglesby, D. (2009). Evidence from coseismic slip gradients for dynamic control on rupture propagation and arrest through stepovers. *Journal of Geophysical Research: Solid Earth*, *114*(B2).

Field, E. H., Arrowsmith, R. J., Biasi, G. P., Bird, P., Dawson, T. E., Felzer, K. R., . . . others (2014). Uniform California earthquake rupture forecast, version 3 (UCERF3)—The time-independent model. *Bulletin of the Seismological Society of America*, *104*(3), 1122–1180.

Finzi, Y., & Langer, S. (2012). Damage in step-overs may enable large cascading earthquakes. *Geophysical Research Letters*, *39*(16).

Fliss, S., Bhat, H. S., Dmowska, R., & Rice, J. R. (2005). Fault branching and rupture directivity. *Journal of Geophysical Research: Solid Earth*, *110*(B6).

Freed, A. M. (2005). Earthquake triggering by static, dynamic, and postseismic stress transfer. *Annu. Rev. Earth Planet. Sci.*, *33*, 335–367.

Galis, M., Ampuero, J. P., Mai, P. M., & Cappa, F. (2017). Induced seismicity provides insight into why earthquake ruptures stop. *Science advances*, *3*(12), eaap7528.

Galis, M., Ampuero, J.-P., Mai, P. M., & Kristek, J. (2019). Initiation and arrest of earthquake ruptures due to elongated overstressed regions. *Geophysical Journal International*, *217*(3), 1783–1797.

Galis, M., Pelties, C., Kristek, J., Moczo, P., Ampuero, J.-P., & Mai, P. M. (2015). On the initiation of sustained slip-weakening ruptures by localized stresses. *Geophysical Journal International*, *200*(2), 890–909. doi: 10.1093/gji/ggu436

Halchuk, S., Allen, T., Adams, J., & Onur, T. (2019). Contribution of the leech river valley-devil's mountain fault system to seismic hazard in victoria, bc.

Hamling, I. J., Hreinsdóttir, S., Clark, K., Elliott, J., Liang, C., Fielding, E., . . . others (2017). Complex multifault rupture during the 2016 Mw 7.8 Kaikōura earthquake, New Zealand. *Science*, *356*(6334), eaam7194.

Harris, R. A., Archuleta, R. J., & Day, S. M. (1991). Fault steps and the dynamic rupture process: 2-D numerical simulations of a spontaneously propagating shear fracture. *Geophysical Research Letters*, *18*(5), 893–896.

Harris, R. A., Barall, M., Aagaard, B., Ma, S., Roten, D., Olsen, K., . . . others (2018). A suite of exercises for verifying dynamic earthquake rupture codes. *Seismological Research Letters*, *89*(3), 1146–1162.

Harris, R. A., & Day, S. M. (1993). Dynamics of fault interaction: Parallel strike-slip faults. *Journal of Geophysical Research: Solid Earth*, *98*(B3), 4461–4472.

Harris, R. A., & Day, S. M. (1999). Dynamic 3D simulations of earthquakes on en echelon faults. *Geophysical Research Letters*, *26*(14), 2089–2092.

Hollingsworth, J., Ye, L., & Avouac, J.-P. (2017). Dynamically triggered slip on a splay fault in the Mw 7.8, 2016 Kaikoura (New Zealand) earthquake. *Geophysical Research Letters*, *44*(8), 3517–3525.

Hu, F., Zhang, Z., & Chen, X. (2016). Investigation of earthquake jump distance for strike-slip step overs based on 3-d dynamic rupture simulations in an elastic half-space. *Journal of Geophysical Research: Solid Earth*, *121*(2), 994–1006.

Huang, Y. (2018). Earthquake rupture in fault zones with along-strike material heterogeneity. *Journal of Geophysical Research: Solid Earth*, *123*(11), 9884–9898.

Huang, Y., Ampuero, J.-P., & Helmberger, D. V. (2014). Earthquake ruptures modulated by waves in damaged fault zones. *Journal of Geophysical Research: Solid Earth*, *119*(4), 3133–3154.

Ida, Y. (1972). Cohesive force across the tip of a longitudinal-shear crack and Grif-

fith's specific surface energy.   *Journal of Geophysical Research*, *77*(20), 3796–
3805.

Ide, S., & Takeo, M.   (1997).   Determination of constitutive relations of fault slip
based on seismic wave analysis.   *Journal of Geophysical Research: Solid Earth*,
102(B12), 27379–27391.

Johnson, S. Y., Dadisman, S. V., Childs, J. R., & Stanley, W. D. (1999). Active tec-
tonics of the Seattle fault and central Puget Sound, Washington—Implications
for earthquake hazards. *Geological Society of America Bulletin*, *111*(7), 1042–
1053.

Johnson, S. Y., Dadisman, S. V., Mosher, D. C., Blakely, R. J., & Childs, J. R.
(2001).   *Active tectonics of the devils mountain fault and related structures,
northern puget lowland and eastern strait of juan de fuca region, pacific north-
west* (Tech. Rep.).

Kaneko, Y., & Lapusta, N.   (2010).   Supershear transition due to a free surface in
3-d simulations of spontaneous dynamic rupture on vertical strike-slip faults.
Tectonophysics, *493*(3-4), 272–284.

Kaneko, Y., Lapusta, N., & Ampuero, J.-P.   (2008).   Spectral element modeling of
spontaneous earthquake rupture on rate and state faults: Effect of velocity-
strengthening friction at shallow depths.   *Journal of Geophysical Research:
Solid Earth*, *113*(B9).

Kase, Y., & Kuge, K.   (2001).   Rupture propagation beyond fault discontinuities:
significance of fault strike and location.   *Geophysical Journal International*,
147(2), 330–342.

Kilb, D., Gomberg, J., & Bodin, P. (2000). Triggering of earthquake aftershocks by
dynamic stresses. *Nature*, *408*(6812), 570–574.

Kilb, D., Gomberg, J., & Bodin, P.   (2002).   Aftershock triggering by complete
coulomb stress changes.   *Journal of Geophysical Research: Solid Earth*,
107(B4), ESE–2.

King, G. C., Stein, R. S., & Lin, J. (1994). Static stress changes and the triggering
of earthquakes. *Bulletin of the Seismological Society of America*, *84*(3), 935–
953.

Kukovica, J., Ghofrani, H., Molnar, S., & Assatourians, K.   (2019).   Probabilistic
Seismic Hazard Analysis of Victoria, British Columbia: Considering an Active

Fault Zone in the Nearby Leech River Valley. *Bulletin of the Seismological Society of America*, *109*(5), 2050–2062.

Li, G., Liu, Y., Regalla, C., & Morell, K. D. (2018). Seismicity relocation and fault structure near the Leech River fault zone, southern Vancouver Island. *Journal of Geophysical Research: Solid Earth*, *123*(4), 2841–2855.

Liu, C., Lay, T., Brodsky, E. E., Dascher-Cousineau, K., & Xiong, X. (2019). Co-seismic Rupture Process of the Large 2019 Ridgecrest Earthquakes From Joint Inversion of Geodetic and Seismological Observations. *Geophysical Research Letters*, *46*(21), 11820–11829.

Lozos, J. C., Dieterich, J. H., & Oglesby, D. D. (2014). The effects of d 0 on rupture propagation on fault stepovers. *Bulletin of the Seismological Society of America*, *104*(4), 1947–1953.

Ma, S., & Andrews, D. (2010). Inelastic off-fault response and three-dimensional dynamics of earthquake rupture on a strike-slip fault. *Journal of Geophysical Research: Solid Earth*, *115*(B4).

MacLeod, N., Tiffin, D., Snavely Jr, P., & Currie, R. (1977). Geologic interpretation of magnetic and gravity anomalies in the strait of juan de fuca, us–canada. *Canadian Journal of Earth Sciences*, *14*(2), 223–238.

Mai, P. M., & Beroza, G. C. (2002). A spatial random field model to characterize complexity in earthquake slip. *Journal of Geophysical Research: Solid Earth*, *107*(B11), ESE–10.

Manighetti, I., Campillo, M., Bouley, S., & Cotton, F. (2007). Earthquake scaling, fault segmentation, and structural maturity. *Earth and Planetary Science Letters*, *253*(3-4), 429–438.

Manighetti, I., Campillo, M., Sammis, C., Mai, P., & King, G. (2005). Evidence for self-similar, triangular slip distributions on earthquakes: Implications for earthquake and fault mechanics. *Journal of Geophysical Research: Solid Earth*, *110*(B5).

Manighetti, I., Caulet, C., De Barros, L., Perrin, C., Cappa, F., & Gaudemer, Y. (2015). Generic along-strike segmentation of a far normal faults, e ast a frica: Implications on fault growth and stress heterogeneity on seismogenic fault planes. *Geochemistry, Geophysics, Geosystems*, *16*(2), 443–467.

Manighetti, I., King, G., & Sammis, C. G. (2004). The role of off-fault damage in

the evolution of normal faults. *Earth and Planetary Science Letters*, *217*(3-4), 399–408.

Manighetti, I., Zigone, D., Campillo, M., & Cotton, F. (2009). Self-similarity of the largest-scale segmentation of the faults: Implications for earthquake behavior. *Earth and Planetary Science Letters*, *288*(3-4), 370–381.

Marone, C. (1998). Laboratory-derived friction laws and their application to seismic faulting. *Annual Review of Earth and Planetary Sciences*, *26*(1), 643–696.

Marone, C., & Kilgore, B. (1993). Scaling of the critical slip distance for seismic faulting with shear strain in fault zones. *Nature*, *362*(6421), 618–621.

Massey, N., MacIntyre, D., Desjardins, P., & Cooney, R. (2005). Digital map of British Columbia: whole province. *BC ministry of energy and mines, GeoFile*, *1*.

McGill, S. F., & Rubin, C. M. (1999). Surficial slip distribution on the central emerson fault during the june 28, 1992, landers earthquake, california. *Journal of Geophysical Research: Solid Earth*, *104*(B3), 4811–4833.

Mikumo, T., Olsen, K. B., Fukuyama, E., & Yagi, Y. (2003). Stress-breakdown time and slip-weakening distance inferred from slip-velocity functions on earthquake faults. *Bulletin of the Seismological Society of America*, *93*(1), 264–282.

Molnar, S., Cassidy, J. F., Olsen, K. B., Dosso, S. E., & He, J. (2014). Earthquake ground motion and 3D Georgia basin amplification in southwest British Columbia: Shallow blind-thrust scenario earthquakes. *Bulletin of the Seismological Society of America*, *104*(1), 321–335.

Morell, K. D., Regalla, C., Amos, C., Bennett, S., Leonard, L., Graham, A., . . . Telka, A. (2018). Holocene Surface Rupture History of an Active Forearc Fault Redefines Seismic Hazard in Southwestern British Columbia, Canada. *Geophysical Research Letters*, *45*(21), 11,605-11,611. doi: 10.1029/2018GL078711

Morell, K. D., Regalla, C., Leonard, L. J., Amos, C., & Levson, V. (2017). Quaternary rupture of a crustal fault beneath Victoria, British Columbia, Canada. *GSA Today*, *27*(3), 4–10.

Nissen, E., Elliott, J., Sloan, R., Craig, T., Funning, G., Hutko, A., . . . Wright, T. (2016). Limitations of rupture forecasting exposed by instantaneously triggered earthquake doublet. *Nature Geoscience*, *9*(4), 330–336.

Oglesby, D. (2008). Rupture termination and jump on parallel offset faults. *Bulletin*

of the Seismological Society of America, *98*(1), 440–447.

Ozacar, A. A., & Beck, S. L. (2004). The 2002 denali fault and 2001 kunlun fault earthquakes: complex rupture processes of two large strike-slip events. *Bulletin of the Seismological Society of America, 94*(6B), S278–S292.

Perrin, C., Manighetti, I., Ampuero, J.-P., Cappa, F., & Gaudemer, Y. (2016). Location of largest earthquake slip and fast rupture controlled by along-strike change in fault structural maturity due to fault growth. *Journal of Geophysical Research: Solid Earth, 121*(5), 3666-3685. doi: 10.1002/2015JB012671

Perrin, C., Manighetti, I., & Gaudemer, Y. (2016). Off-fault tip splay networks: A genetic and generic property of faults indicative of their long-term propagation. *Comptes Rendus Geoscience, 348*(1), 52–60.

Ripperger, J., Ampuero, J.-P., Mai, P., & Giardini, D. (2007). Earthquake source characteristics from dynamic rupture with constrained stochastic fault stress. *Journal of Geophysical Research: Solid Earth, 112*(B4).

Ripperger, J., Mai, P., & Ampuero, J.-P. (2008). Variability of near-field ground motion from dynamic earthquake rupture simulations. *Bulletin of the seismological society of America, 98*(3), 1207–1228.

Ross, Z. E., Idini, B., Jia, Z., Stephenson, O. L., Zhong, M., Wang, X., ... others (2019). Hierarchical interlocked orthogonal faulting in the 2019 Ridgecrest earthquake sequence. *Science, 366*(6463), 346–351.

Ryan, K. J., & Oglesby, D. D. (2014). Dynamically modeling fault step overs using various friction laws. *Journal of Geophysical Research: Solid Earth, 119*(7), 5814–5829.

Savage, H. M., & Brodsky, E. E. (2011). Collateral damage: Evolution with displacement of fracture distribution and secondary fault strands in fault damage zones. *Journal of Geophysical Research: Solid Earth, 116*(B3).

Savage, H. M., & Cooke, M. L. (2010). Unlocking the effects of friction on fault damage zones. *Journal of Structural Geology, 32*(11), 1732–1741.

Savard, G., Bostock, M. G., & Christensen, N. I. (2018). Seismicity, metamorphism, and fluid evolution across the Northern Cascadia fore arc. *Geochemistry, Geophysics, Geosystems, 19*(6), 1881–1897.

Sherrod, B. L., Blakely, R. J., Weaver, C. S., Kelsey, H., Barnett, E., & Wells, R. (2005). Holocene fault scarps and shallow magnetic anomalies along the south-

ern whidbey island fault zone near woodinville, washington. *US Geol. Surv. Open File Rep*, *1136*, 36.

Sherrod, B. L., Blakely, R. J., Weaver, C. S., Kelsey, H. M., Barnett, E., Liberty, L., ... Pape, K. (2008). Finding concealed active faults: Extending the southern Whidbey Island fault across the Puget Lowland, Washington. *Journal of Geophysical Research: Solid Earth*, *113*(B5).

Sibson, R. H. (1986). Rupture interaction with fault jogs. *Earthquake Source Mechanics*, *37*, 157–167.

Stern, A. R. (2016). Fault Interaction within Restraining Bend Fault Systems.

Tarnowski, J. M. (2017). The Effects of Dynamic Stress on Fault Interaction and Earthquake Triggering in the San Gorgonio Pass and San Jacinto, CA Regions.

Toda, S., Stein, R. S., Reasenberg, P. A., Dieterich, J. H., & Yoshida, A. (1998). Stress transferred by the 1995 Mw = 6.9 Kobe, Japan, shock: Effect on aftershocks and future earthquake probabilities. *Journal of Geophysical Research: Solid Earth*, *103*(B10), 24543-24565. doi: 10.1029/98JB00765

Uenishi, K. (2009). On the mechanical destabilization of a three-dimensional displacement-softening plane of weakness. In *Proceedings of the 38th symposium on rock mechanics* (pp. 332–337).

Verdecchia, A., Pace, B., Visini, F., Scotti, O., Peruzza, L., & Benedetti, L. (2018). The role of viscoelastic stress transfer in long-term earthquake cascades: Insights after the central Italy 2016–2017 seismic sequence. *Tectonics*, *37*(10), 3411–3428.

Voisin, C., Cotton, F., & Di Carli, S. (2004). A unified model for dynamic and static stress triggering of aftershocks, antishocks, remote seismicity, creep events, and multisegmented rupture. *Journal of Geophysical Research: Solid Earth*, *109*(B6). doi: 10.1029/2003JB002886

Walsh, J., Bailey, W., Childs, C., Nicol, A., & Bonson, C. (2003). Formation of segmented normal faults: a 3-d perspective. *Journal of Structural Geology*, *25*(8), 1251–1262.

Weng, H., & Yang, H. (2017). Seismogenic width controls aspect ratios of earthquake ruptures. *Geophysical Research Letters*, *44*(6), 2725-2732. doi: 10.1002/2016GL072168

1065   Wesnousky, S. G. (1988). Seismological and structural evolution of strike-slip faults.
1066   *Nature*, *335*(6188), 340–343.

1067   Wesnousky, S. G. (2006). Predicting the endpoints of earthquake ruptures. *Nature*,
1068   *444*(7117), 358–360.

1069   Xu, J., Zhang, H., & Chen, X.   (2015).   Rupture phase diagrams for a planar fault
1070   in 3-D full-space and half-space.   *Geophysical Journal International*, *202*(3),
1071   2194–2206.

1072   Yang, H., Yao, S., He, B., Newman, A. V., & Weng, H. (2019). Deriving rupture sce-
1073   narios from interseismic locking distributions along the subduction megathrust.
1074   *Journal of Geophysical Research: Solid Earth*, *124*(10), 10376–10392.

1075   Zaleski, M. P.   (2014).   *Earthquake Loss Estimates, Greater Victoria, British*
1076   *Columbia* (Unpublished master's thesis). Simon Fraser University.

1077   Zielke, O., Galis, M., & Mai, P. M.   (2017).   Fault roughness and strength hetero-
1078   geneity control earthquake size and stress drop.   *Geophysical Research Letters*,
1079   *44*(2), 777–783.

Table 1.   List of simulation parameters

Parameter	Value
P wave velocity, V_p (m/s)	6000
S wave velocity, V_s (m/s)	3464
Poisson's ratio, ν	0.25
Shear modulus, G (GPa)	32
Static friction coefficient, μ_s	0.6
Dynamic friction coefficient, μ_d	0.2
Initial normal stress, σ_{n0} (MPa)	25
Static friction, τ_s (MPa)	15
Dynamic friction, τ_d (MPa)	5
Initial shear stress within the nucleation zone, τ_0^i (MPa)	16.5
Characteristic slip-weakening distance, d_0 (m)	0.4
LRF length, L_1 (km)	50
LRF width, W_1 (km)	34.6
LRF dip angle, θ_1	60°
SWIF length, L_2 (km)	30
SWIF width, W_2 (km)	30
SWIF dip angle, θ_2	90°
Overlapping distnace, L (km)	10
LRF burial depth, D_1 (km)	0 - 2
SWIF burial depth, D_2 (km)	0 - 10
Offset distance, L_0 (km)	1 - 10
Nondimensional fault initial shear stress level, S_0	0.5 - 1.5
LRF nucleation patch radius (km)	3
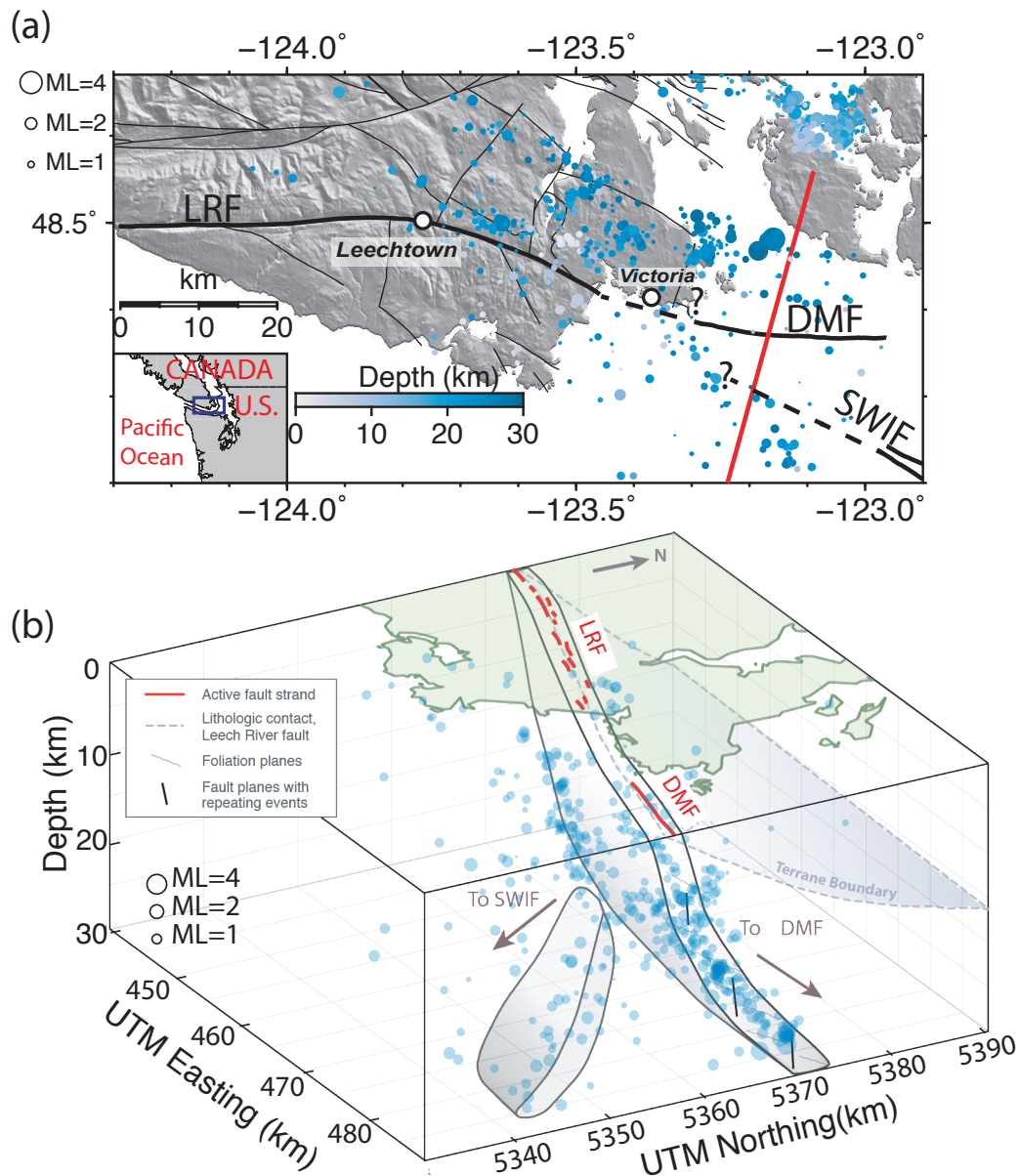
Figure 1. (a) Map of the study area showing relocated crustal earthquakes (depth <30 km) in Li et al. (2018), and mapped faults in British Columbia (Massey et al., 2005). The red line is the transect line in Figure 2b. Dashed lines represent possible extension from the LRF and the SWIF, respectively. The question marks indicate this configuration is based on an educated guess with weak geological evidence. LRF: Leech River fault. SWIF: Southern Whidbey Island fault. DMF: Devils' Mountain fault. (b) Illustration of the LRF step-over system with 3D seismicity. This is an extensional step-over with two right-lateral strike-slip faults.
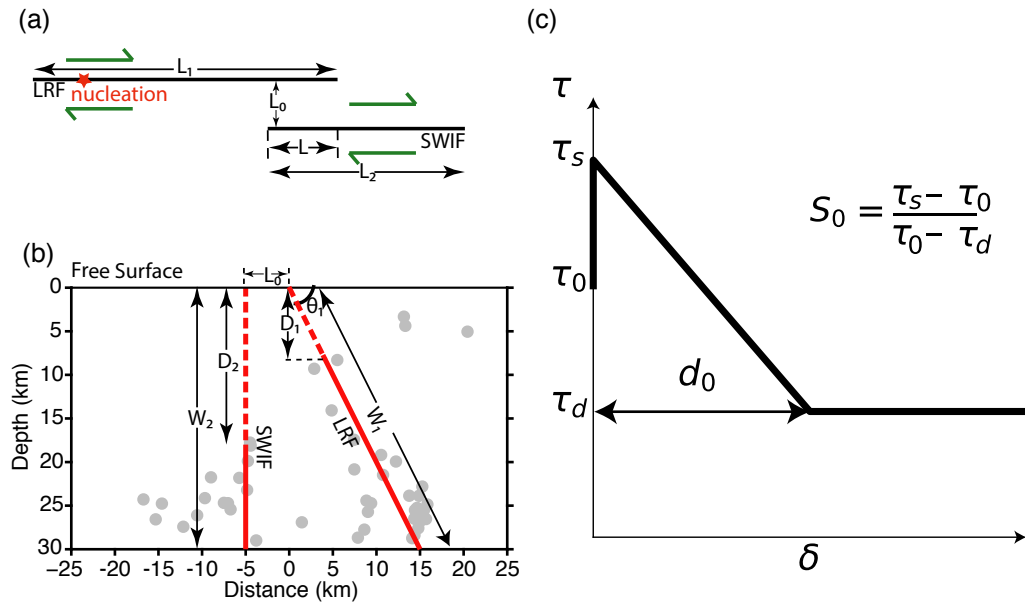
Figure 2. (a)-(b) Illustration of fault step-over geometry model in map view and cross-sectional view along the red line in Figure 1a. Earthquakes within 5 km to the transect line are plotted in (b). The dashed lines represent the unfaulted continuations of fault slip surfaces up to the free surface. The scale of D_1 and D_2 in the figure are chosen only for illustration purposes; see parameter choices in Table 1. (c) A diagram showing the slip-weakening law and S_0. δ is the cumulative slip and τ is the shear stress on the fault.
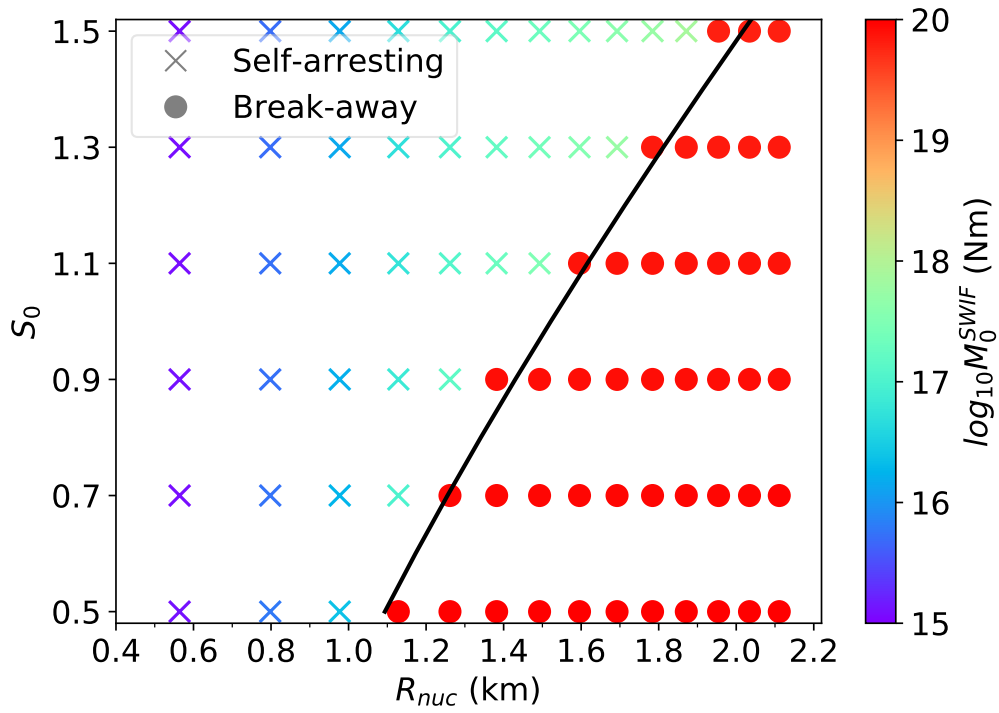
Figure 3. A phase diagram demonstrating the influence of R_{nuc} and initial stress level S_0 on rupture scenarios observed on a single fault modeled after the SWIF geometry. The black line marks the theoretical boundary estimated in Galis et al. (2015).
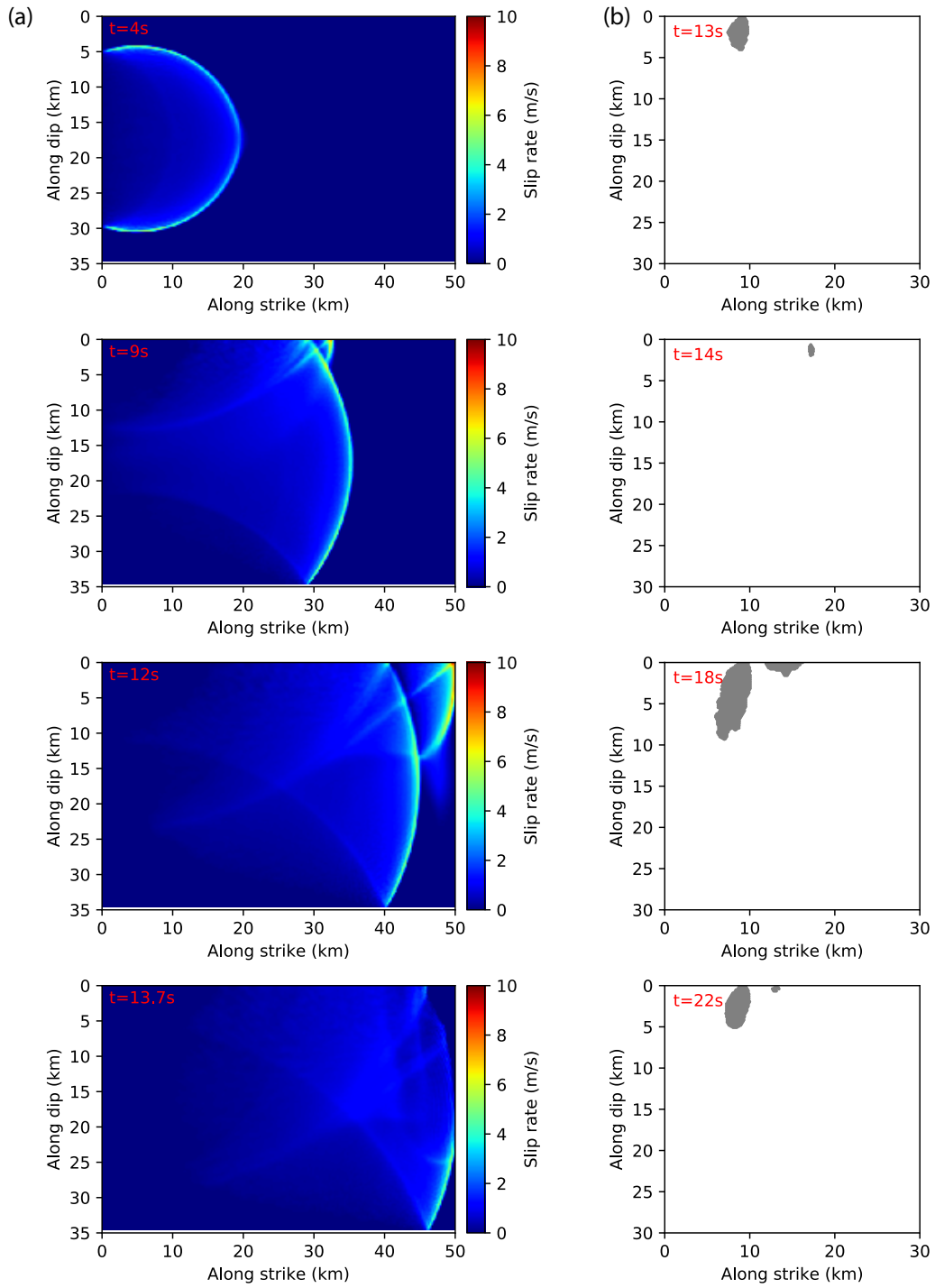
Figure 4. Simulation snapshots for $L_0 = 1$ km, $S_0 = 0.7$, $D_1 = 0$ km and $D_2 = 0$ km at different times for (a) the slip rates on the LRF and (b) the development of OSZ (shaded region) on the SWIF plane. $t = 0$ s indicates the initialization time of the LRF rupture.
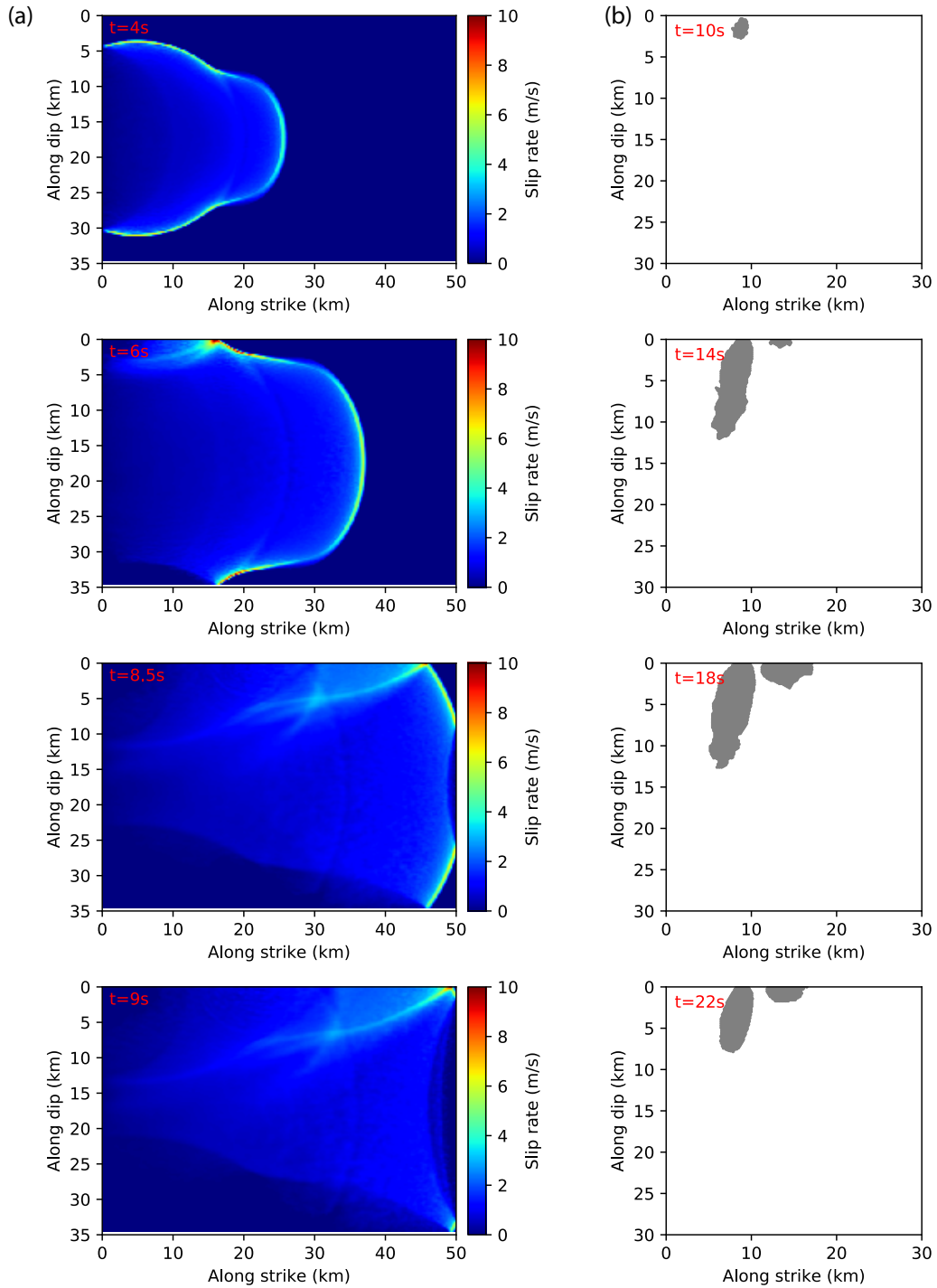
Figure 5. Similar to Figure 4, but for $L_0 = 1$ km, $S_0 = 0.5$, $D_1 = 0$ km and $D_2 = 0$ km.
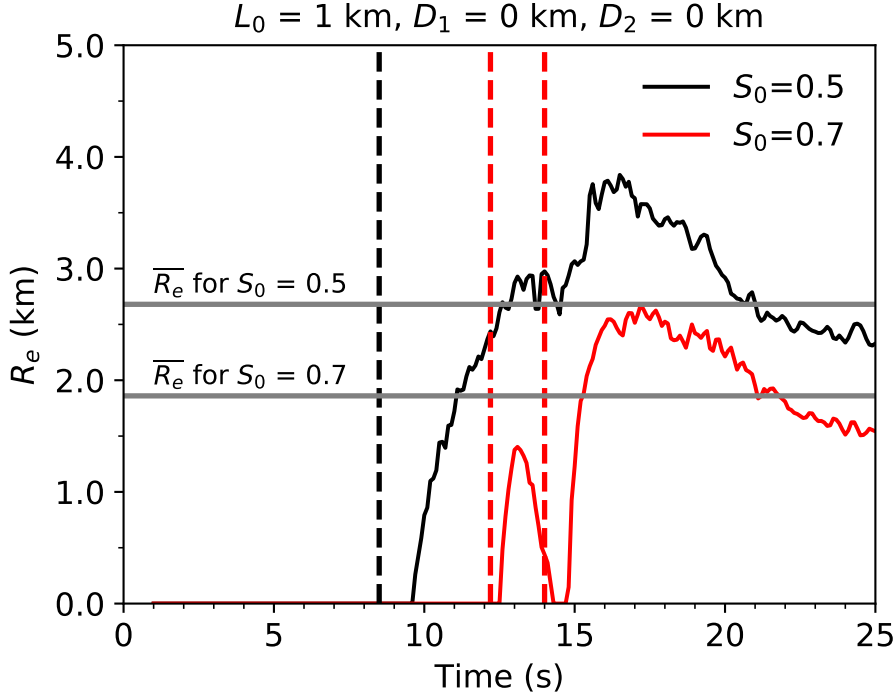
Figure 6. Curves showing the variation of R_e as a function of time for examples in Figures 4 and 5. The black and red vertical lines represent when the LRF rupture fronts meet the fault edge for simulations with $S_0 = 0.5$ and $S_0 = 0.7$, respectively. Horizontal grey lines show $\overline{R_e}$ for two simulation cases.
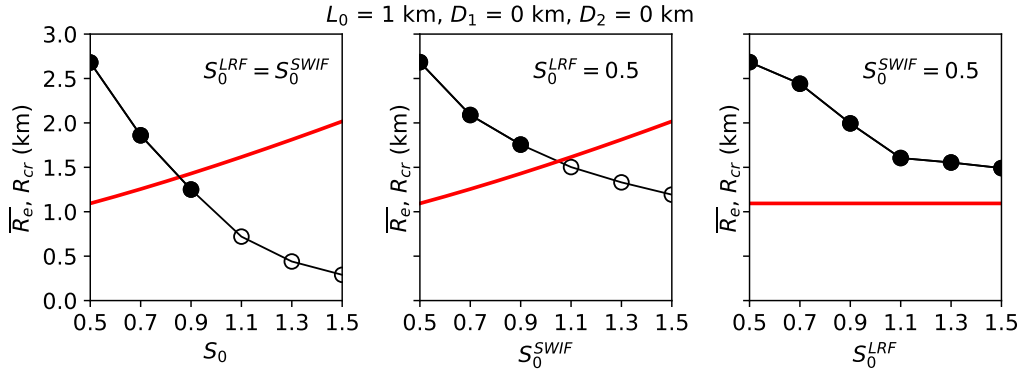
Figure 7. Curves showing $\overline{R_e}$ as a function of S_0 (when both faults are equally stressed), S_0^{SWIF} and S_0^{LRF} when $L_1 = 1$ km, $D_1 = 0$ km and $D_2 = 0$ km. The red lines represent R_{cr} estimated by Equation 7. Solid and open circles represent break-away and self-arresting scenarios, respectively.
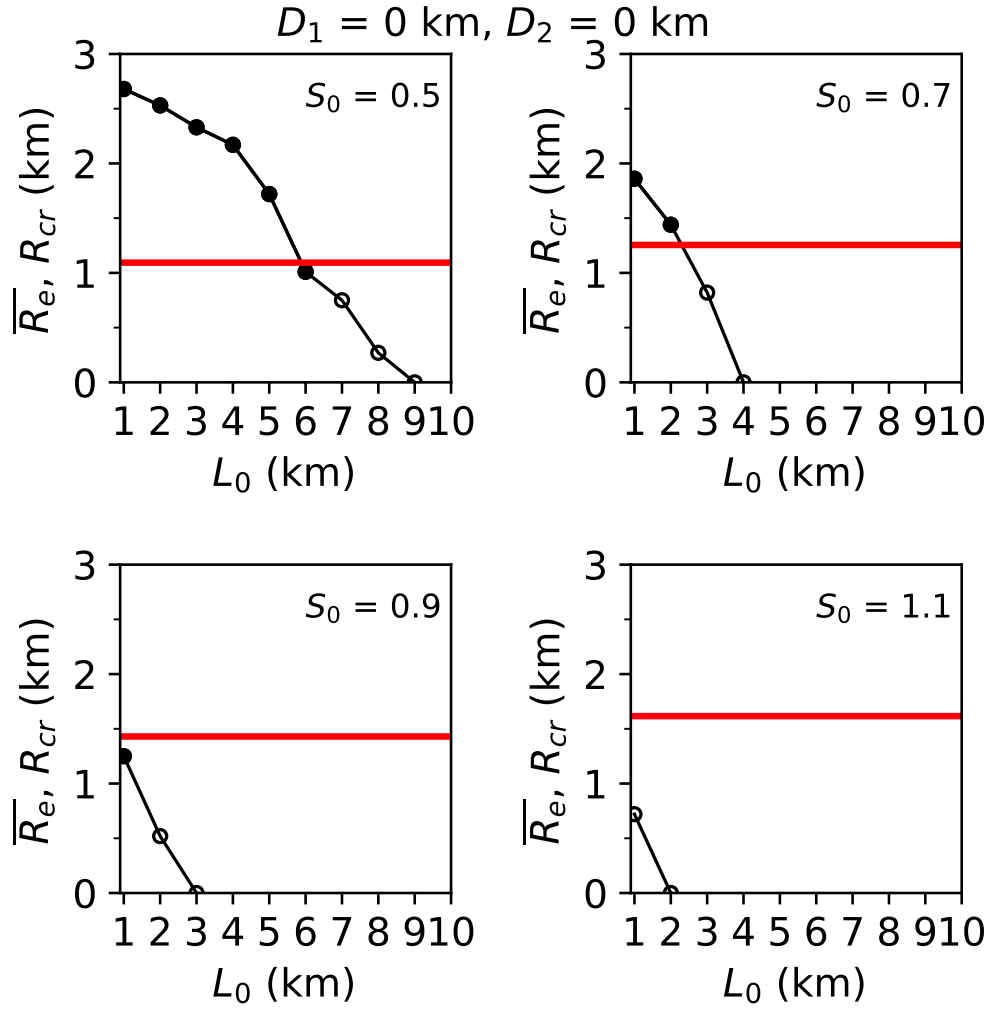
Figure 8. Curves showing $\overline{R_e}$ as a function of offset distance with different initial shear stress levels when $D_1 = 0$ km and $D_2 = 0$ km. The red lines represent R_{cr} at given S_0^{SWIF} estimated by Equation 7. Solid and open circles represent break-away and self-arresting scenarios, respectively.
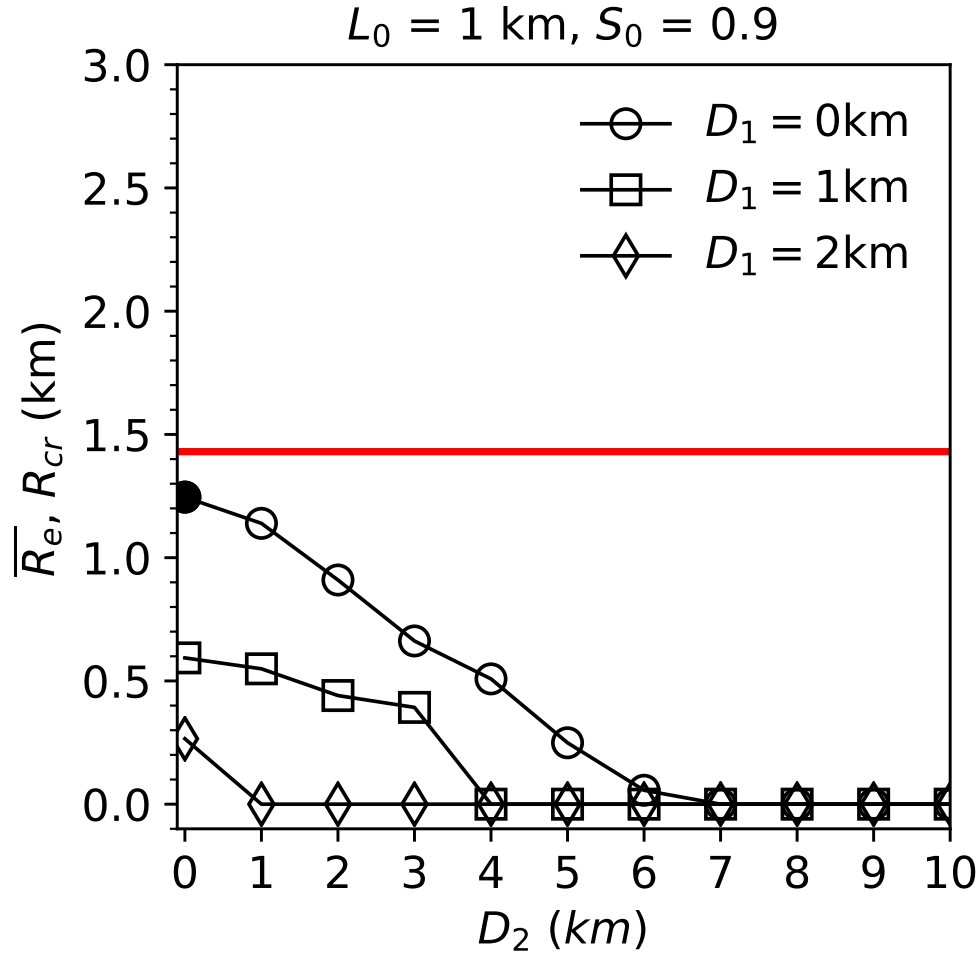
Figure 9. Curves showing $\overline{R_e}$ as a function of D_2 for different burial depths of the LRF. The red line shows R_{cr} for $S_0^{SWIF} = 0.9$. Solid and open symbols represent break-away and self-arresting scenarios, respectively.
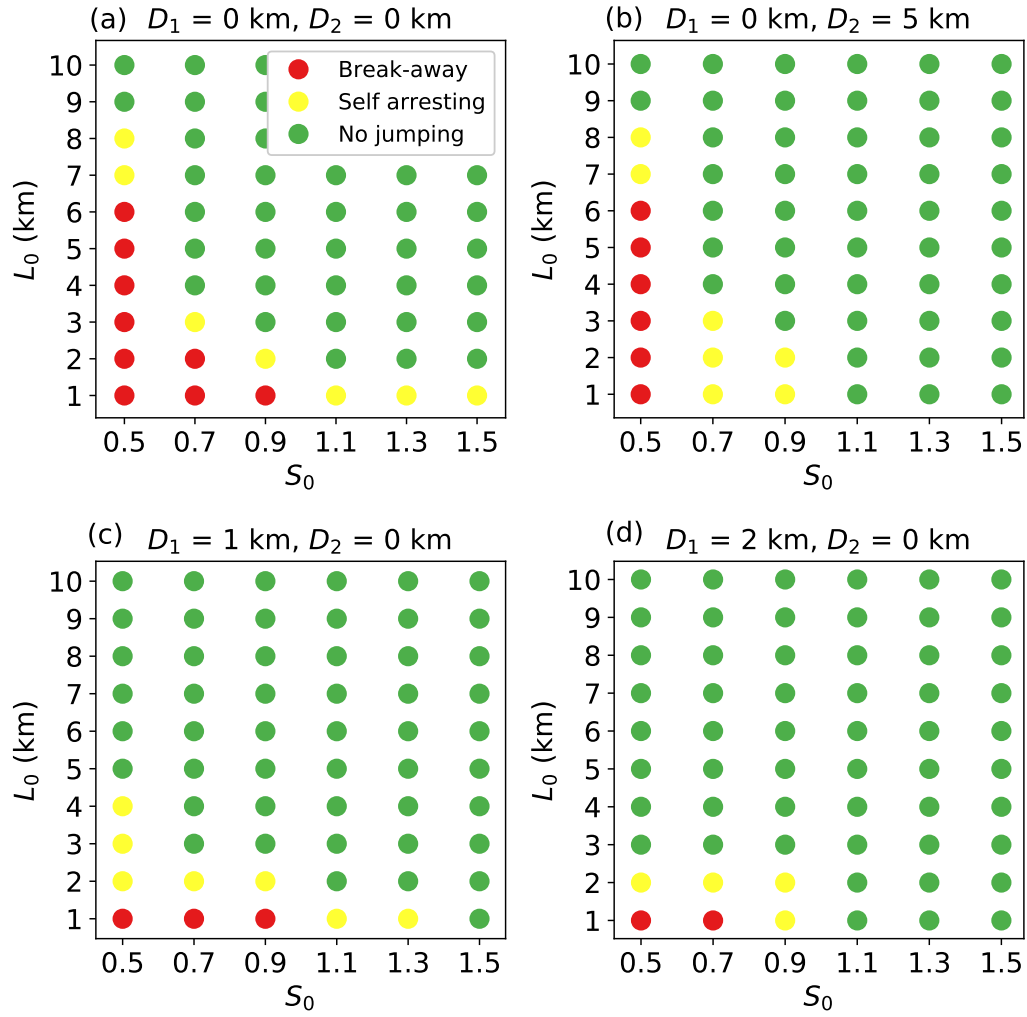
**Figure 10.** A phase diagram showing the effect of different parameters on rupture jumping scenario.
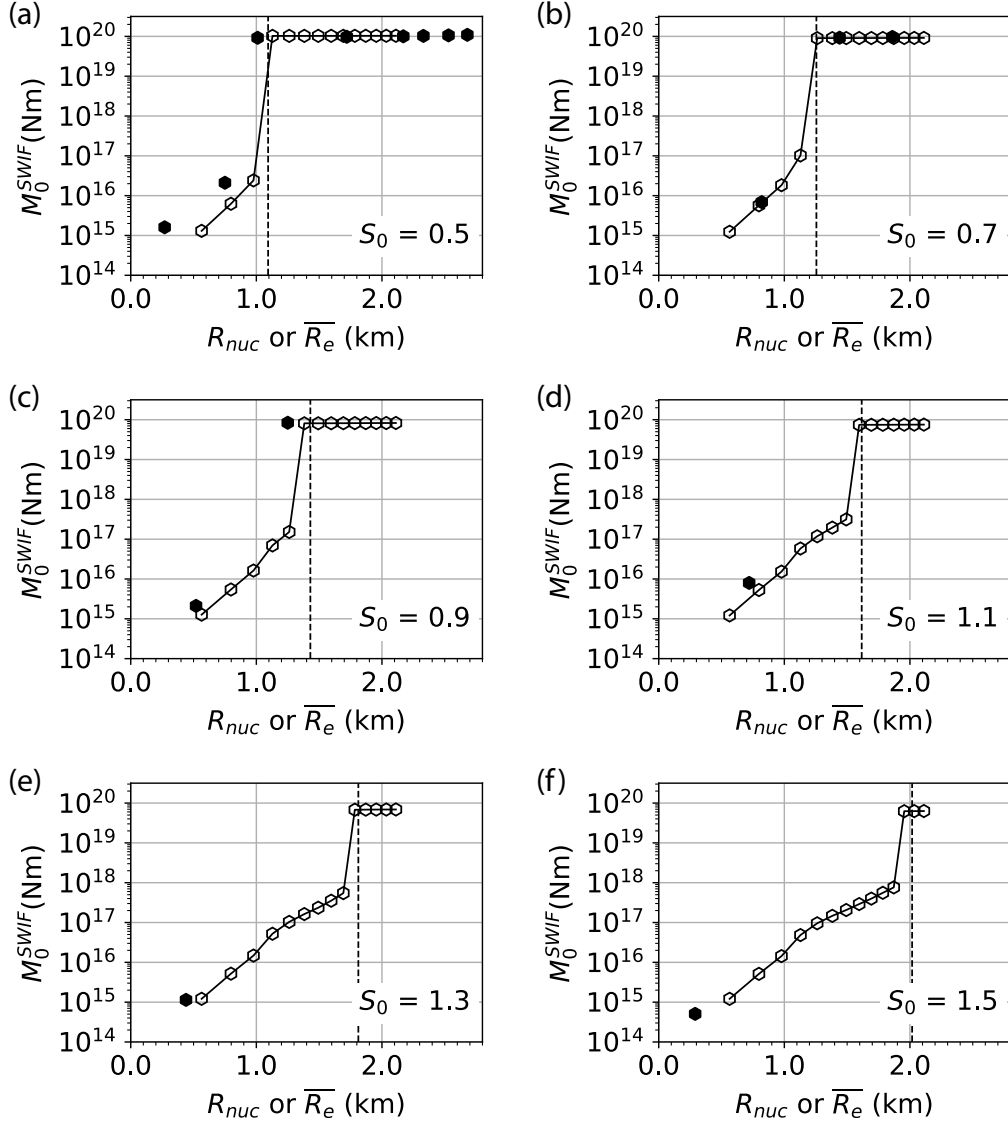
Figure 11. (a)-(f) Curves showing final SWIF seismic moment (M_0^{SWIF}) as a function of R_{nuc} (the radius of nucleation patch used for rupture initialization on a single SWIF) or $\overline{R_e}$ (the time-averaged OSZ size observed on the SWIF in simulations considering rupture on both faults in the step-over system). Fixed model parameters are $L_0 = 1$ km, $D_1 = 0$ km, and $D_2 = 0$ km. The vertical black dashed line in each subplot represent R_{cr} estimated by Equation 7. Lines with open markers represent the (R_{nuc}, M_0^{SWIF}) data set and solid markers represent the ($\overline{R_e}$, M_0^{SWIF}).
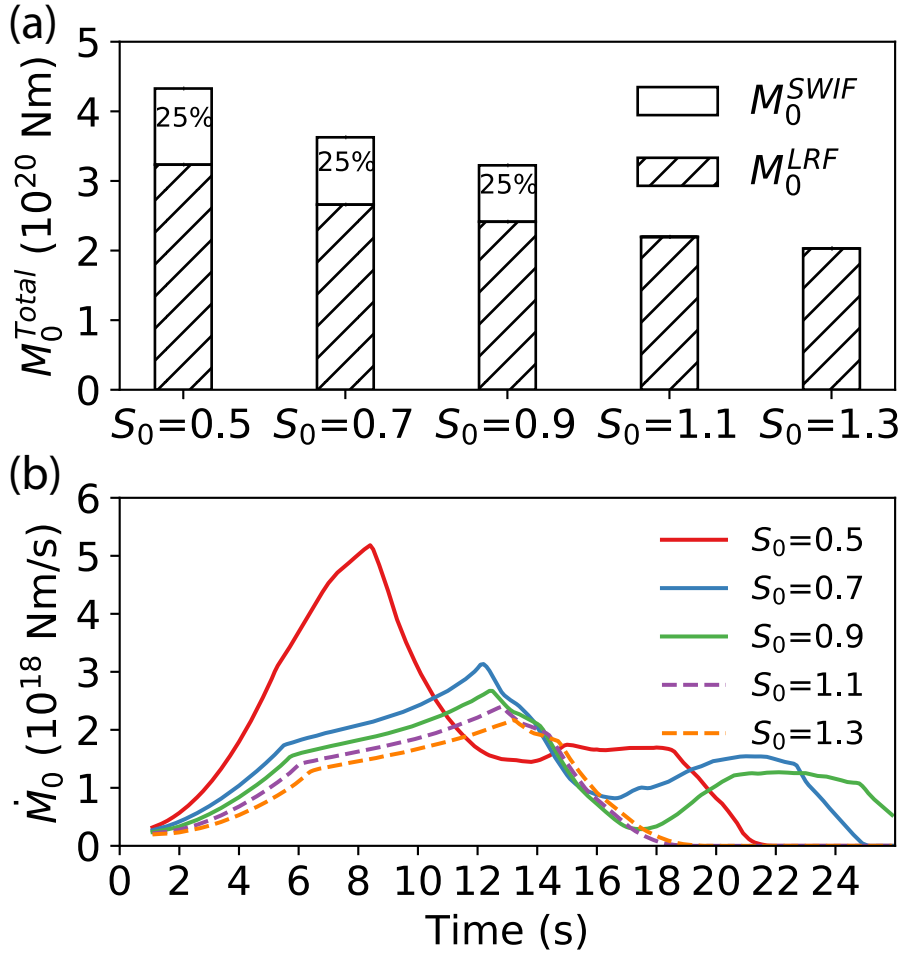
Figure 12. (a) Total seismic moment (M_0^{Total}) released and (b) moment release rate $(\dot{M}_0)$ as a function of time at different initial stress levels, when $L_0 = 1$ km, $D_1 = 0$ km and $D_2 = 0$ km. The hatched and open area in (a) represent the contribution from the LRF and the SWIF, respectively. Solid lines in (b) denote the break-away ruptures on the SWIF, and dashed lines denote self-arresting ones.